Available online at www.sciencedirect.com

ScienceDirect

Underground Space 25 (2025) 132–155

www.keaipublishing.com/undsp

Research Paper

Spatial motion patterns and force transmission characteristics of muck particles in EPB shield tunneling: An FDM–DEM coupling analysis

Yuxiang Yao, Yong Fang *, Chuan He, Gongyun Xu, Zhigang Yao, Xiongyu Hu

Key Laboratory of Transportation Tunnel Engineering, Ministry of Education, Southwest Jiaotong University, Chengdu 610031, China

Received 10 January 2025; received in revised form 27 April 2025; accepted 31 May 2025
Available online 16 September 2025

Abstract

Earth pressure balance (EPB) shield tunneling in sandy cobble strata often encounters challenges such as muck stagnation, severe tool wear, difficulties in chamber pressure control, and low excavation efficiency. To address these issues, this study proposes a novel gradient stress construction strategy based on rigid wall boundaries by integrating the finite difference method (FDM) and the discrete element method (DEM), and establishes a refined FDM–DEM coupled shield tunneling model. Using this model, the pressure distribution and load transfer mechanisms at the excavation face and within the chamber, as well as the motion trajectories, velocities, and spatial distribution of muck particles, are analyzed in detail. The results indicate that: (1) The pressure at the cutterhead spokes is lower than that at the cutterhead openings; the muck pressure within the chamber exhibits significant radial gradient variations, with distinct differences between the left and right sides. (2) The average pressure in the upper regions of both the left and right sides of the chamber is nearly equal, with a stable pressure transmission coefficient of approximately 0.8. An under-pressure advancement strategy is recommended to avoid ground heave. (3) The muck particles follow spiral trajectories, forming dual-vortex stagnation zones in the central region of the cutterhead (0–0.2D, where D denotes the cutterhead diameter) and the support column region of the chamber (0–0.25D). The installation of radial mixing rods on the cutterhead shaft is suggested to improve muck flowability. This study provides new insights for optimizing cutterhead and chamber design, offering significant implications for enhancing the efficiency of shield tunneling construction.

Keywords: EPB shield; Sandy cobble strata; Spatial motion patterns; Force transmission characteristics

1 Introduction

With the increasing development and utilization of urban underground spaces, earth pressure balance (EPB) shields have been widely adopted in urban metro and cross-river/sea tunnel projects due to their advanced control technologies, high construction safety, and minimal environmental impact (Li et al., 2023; Xie et al., 2024). Sandy cobble strata, a common and complex ground type in shield tunneling, exhibit distinct physical and mechanical properties that significantly influence tunneling performance, as illustrated in Fig. 1. These strata are primarily composed of sand and cobbles, with particles mainly in point contact, resulting in a loose structure characterized by high porosity and low cohesion, which leads to poor overall stability. This loose structure complicates the control of face and chamber pressure balance during shield excavation (Yao et al., 2024; H. H. Zhu et al., 2020). Additionally, the large internal friction angle of sandy cobble strata indicates high interparticle frictional resistance, resulting in poor flow plasticity. This property often causes muck stagnation in front of the cutterhead or within the chamber, increasing the difficulty of muck discharge. Moreover, the uniaxial compressive strength of individual

* Corresponding author.
E-mail address: fy980220@swjtu.cn (Y. Fang).
Peer review under the responsibility of Tongji University

https://doi.org/10.1016/j.undsp.2025.05.005

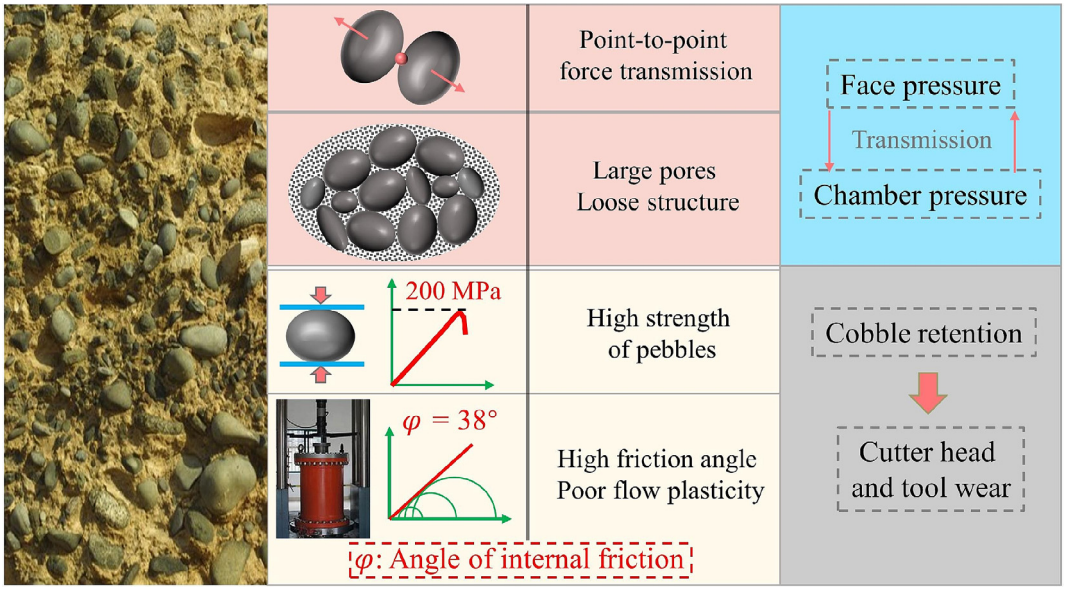

Fig. 1. Characterization of the properties of the sandy cobble stratum.

cobbles can reach up to 200 MPa, indicating their extremely high strength and resistance to fragmentation. These high-strength cobbles not only exacerbate cutterhead tool wear but also increase energy consumption and construction costs. Consequently, EPB shields face numerous challenges when tunneling in such strata, including low excavation efficiency, poor muck discharge, cobble sedimentation, severe tool wear, difficulties in chamber pressure control, and excessive ground settlement (Amoun et al., 2017; Ji et al., 2023). These issues significantly hinder the smooth progress of shield tunneling projects.

During EPB shield tunneling, chamber pressure is a critical parameter for maintaining face stability (Idinger et al., 2011; Hu et al., 2021). As the cutterhead rotates and the screw conveyor discharges muck, the face pressure and chamber pressure exhibit complex dynamic variations (Dang & Meschke, 2020; Xu et al., 2024). Accurately understanding the pressure transmission mechanisms between the face and the chamber not only helps optimize pressure control strategies and improve muck discharge efficiency but also effectively controls ground disturbance and prevents surface collapse (Chen et al., 2019; Yu et al., 2020). Simultaneously, the timely and orderly transport and discharge of cobble particles cut by the cutterhead are directly related to the continuous and efficient advancement of the shield machine. If muck transport is hindered, it may lead to muck accumulation in front of the cutterhead or within the chamber, causing difficulties in muck discharge, accelerated tool wear, and ultimately affecting project progress and construction safety. Therefore, to enhance the adaptability of EPB shields in sandy cobble strata, it is essential to conduct in-depth research on the spatial motion patterns and pressure transmission mechanisms of muck particles during shield tunneling.

Currently, existing model shield devices and testing techniques are insufficient for comprehensively studying and testing the microscopic transport behavior and pressure transmission of muck particles during shield tunneling (Hu et al., 2020; Lin et al., 2021). The discrete element method (DEM) provides a new solution for studying the interaction between geotechnical materials and engineering machinery (Guo et al., 2023; Yi & Yang, 2024). Existing research shows that DEM can simulate the dynamic tunneling process of EPB shields in sandy cobble strata, but related studies have primarily focused on optimizing tunneling parameters, analyzing tunnel face stability, and investigating tool cutting mechanisms (Chen et al., 2011; Duan et al., 2023). Systematic research on the transport characteristics and pressure transmission mechanisms of muck particles during shield tunneling remains limited. Additionally, the computational efficiency of pure DEM significantly decreases when the number of elements exceeds 100 000, which limits its application in practical engineering to some extent (Cheng et al., 2023). In contrast, the finite difference method (FDM), as an effective numerical method, demonstrates advantages in stress analysis and continuity problems of soil, particularly for simulating large-scale ground conditions. The FDM–DEM coupling method combines the strengths of both approaches, enabling the simulation of particle systems while accurately describing the continuity characteristics of soil (Shao et al., 2022). However, the application of this method in dynamic shield tunneling is still in its early stages, and how to precisely study particle motion and pressure transmission mechanisms in sandy cobble strata using coupled models remains an unresolved issue.

In light of this, this study establishes a refined, full-scale three-dimensional FDM–DEM coupled numerical model

for shield tunneling, aiming to investigate the transport patterns, local stagnation characteristics, and force transmission mechanisms of sandy cobble particles in confined spaces. By revealing the dynamic behavior of complex particle systems and soil stress distribution characteristics at the microscopic level, this research seeks to deepen the understanding of the flow guidance characteristics of the cutterhead and the force transmission mechanisms of muck particles. This will provide guidance for the design of cutterhead structures, tool arrangements, chamber configurations, and chamber pressure control, further advancing research on cutterhead selection, tool layout, and chamber pressure control in sandy cobble strata.

2 Project overview and shield machine configuration

2.1 Project overview

The 08th section of Beijing Metro Line 19 is situated in Daxing District, Beijing, China, with the tunnel alignment extending from Xinfadi Station to Caoqiao Station, spanning a total length of 2.38 km (Fig. 2). The construction utilizes an EPB shield machine with a diameter of 6600 mm for tunneling. The tunnel lining comprises precast concrete segments, characterized by an outer diameter of 6400 mm, an inner diameter of 5800 mm, and a width of 1200 mm. According to geological survey data, the tunnel predominantly traverses a sandy cobble stratum composed mainly of pebbles and gravels. The particle size of the cobbles primarily ranges from 30 to 100 mm, with sub-rounded and elliptical shapes being the most prevalent. The interstices between the pebbles are filled with medium to coarse sand. The tunnel burial depth exhibits significant variation, with overburden depths ranging from 13.2 to 29.3 m. The key physical and mechanical properties of the sandy cobble stratum in this section are summarized in Table 1.

2.2 Shield machine configuration

EPB shield machines typically employ two types of cutterheads: spoke-type and panel-type. Spoke-type cutterheads are characterized by a high opening ratio, often exceeding 50%, while panel-type cutterheads exhibit a lower opening ratio, typically ranging from 20% to 40%. For this project, a spoke-type cutterhead with a high opening ratio of approximately 60% was selected. The cutterhead comprises six spokes and incorporates a tool configuration that integrates scrapers, leading tools, and central fishtail tools. The detailed structure is illustrated in Fig. 3, and the relevant technical parameters of the shield machine are summarized in Table 2. A central fishtail tool with a height of 550 mm is installed on the cutterhead surface to enhance cutting and mixing efficiency in the central area, thereby preventing muck accumulation and the formation of mud cakes. Additionally, two types of leading tools are employed: 47 tools with a height of 165 mm and a width of 300 mm, and 12 tools with a height of 165 mm and a width of 200 mm. These tools are arranged in multiple layers to optimize the cutting performance of the cutterhead. The scrapers, designed for soil cutting and stripping, consist of 51 pairs of tools with a protrusion height of 125 mm and a width of 150 mm. They are alternately installed on both sides of each spoke to ensure comprehensive coverage of the cutterhead opening area, thereby eliminating blind spots during excavation. In this project, a belt-type screw conveyor with a pitch and inner diameter of 800 mm and an inclination angle of 25° was implemented.

3 Methods and material properties

3.1 Coupling method

In the coupled simulation using FLAC3D and PFC3D, FLAC3D is employed to model the macroscopic mechanical behavior of the continuous medium, while PFC3D models the macroscopic mechanical behavior of the discrete medium. The coupling process between the two programs involves three modes: wall-zone coupling, wall-structure coupling, and ball-zone coupling. The coupling logic between PFC3D and FLAC3D is managed through an interface at the coupling boundary, which facilitates the transfer of force and velocity data between the two programs. Zhao et al. (2022) compared various coupling modes and found that wall-zone coupling provided superior performance and faster convergence. Consequently, in this study, wall-zone interface coupling is utilized to enable data interaction between the two media. The

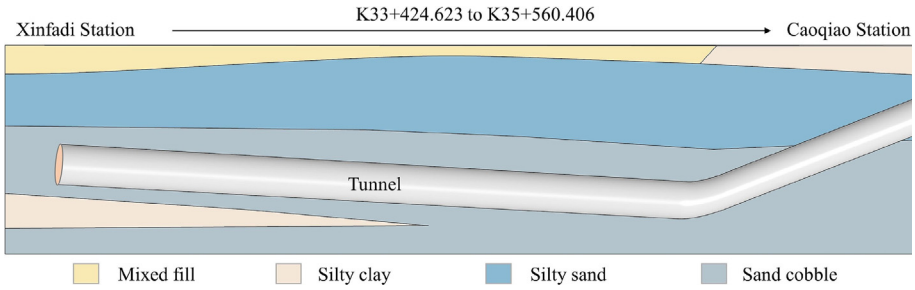

Fig. 2. Geological longitudinal section of the shield tunnel.

Table 1
Physical and mechanical parameters of sandy cobble soil.

Soil type	Weight (kN/m^3)	Cohesion (kPa)	Internal friction angle (°)	Deformation modulus (MPa)	Poisson's ratio	Lateral pressure coefficient (k_0)
Sandy cobble soil	21.0	0	38.0	25.0	0.25	0.30

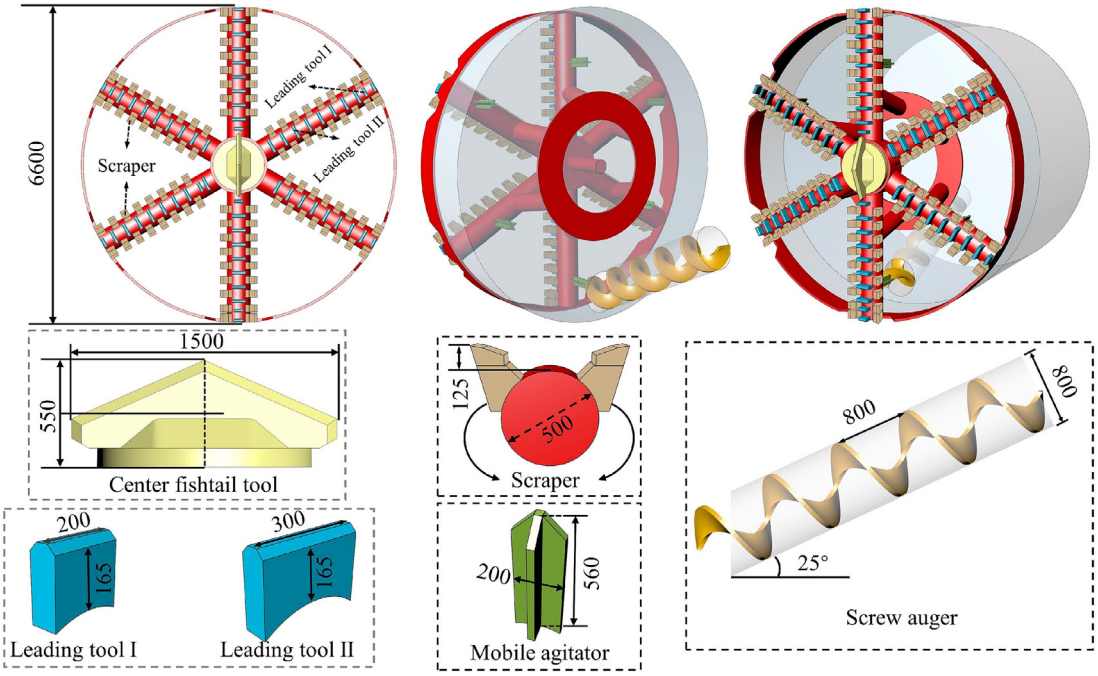

Fig. 3. Geometry model of EPB shield for DEM simulation. (Unit: mm)

Table 2
Components and specifications of the EPB shield model.

Property	Description
Diameter of cutterhead (m)	6.6
Number of spokes	6.0
Opening ratio (%)	66
Length of shield (m)	4.0
Diameter of screw (m)	0.9
Pitch of screw (m)	0.8
Length of screw conveyor (m)	6.0
Inclination of screw conveyor (°)	25.0

fundamental principles of the 3D continuous-discrete coupling approach based on FLAC3D and PFC3D are depicted in Fig. 4.

The coupling between FLAC3D and PFC3D is based on boundary-controlled continuous-discrete interaction. In each iteration of PFC3D, force–displacement criteria are applied to the contacts, and the motion of the granules is governed by Newton's second law, with the positions of both the granules and the boundary walls being continuously updated. The unbalanced forces at the coupling interface are transmitted to FLAC3D through the Socket I/O interface. Upon receiving the updated stress and force data, FLAC3D calculates the new velocity and displacement by solving the equilibrium (motion) equations. These updated displacements are then sent back via the Socket I/O interface to update the boundary conditions, resulting in the motion of the granules in the discrete domain, and the cycle repeats. It is essential to emphasize that the mechanical analysis within this coupling must be performed in large deformation mode, and both the coupling interface and imported boundaries must be discretized into triangular meshes.

3.2 Constitutive model

In this study, the Mohr–Coulomb model was employed to represent the continuous region in the coupled model, while two distinct contact models were introduced in the discrete domain to simulate both the in-situ and conditioned soils. The Mohr–Coulomb model is widely utilized in geotechnical engineering, and its fundamental principles and applications are beyond the scope of this discussion.

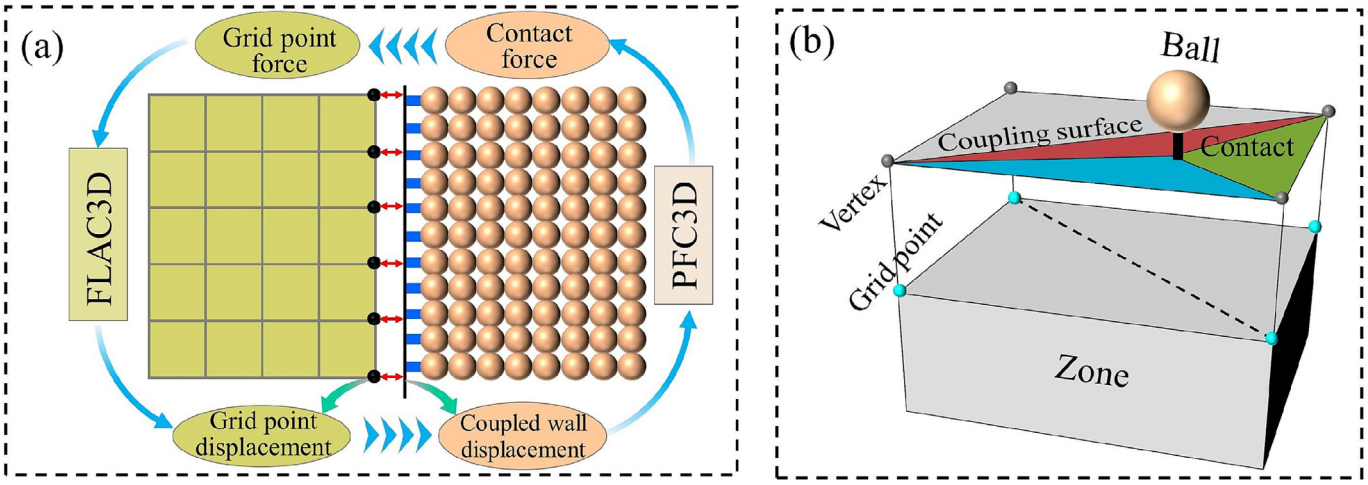

Fig. 4. FDM–DEM coupling method. (a) Data transmission, and (b) a schematic diagram of the wall-zone coupling method.

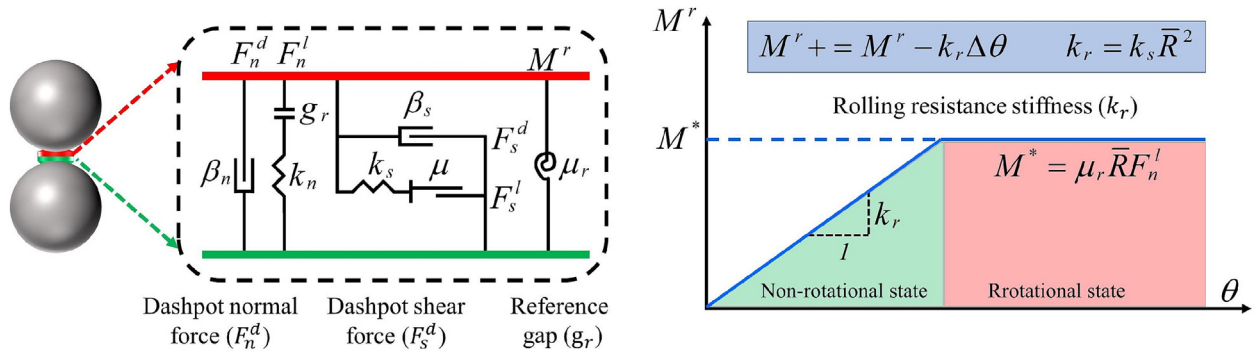

Fig. 5. Behavior and rheological components of the rolling resistance linear model.

To simulate in-situ soil in the discrete domain, the rolling resistance linear (RRlinear) model was employed. This model represents granular materials that do not bond but are capable of transmitting substantial bending moments, such as sandy cobbles and sandy gravel. In the RRlinear model, the contact torque (M^r) is proportional to the angular displacement (θ). As the angular displacement increases, the contact torque also increases, reaching a peak value at which the contact point rotates, after which the torque remains constant. The peak torque (M^*) is determined by the rotation resistance coefficient (μ_r), contact element size ($\bar{R}$), and the linear normal force (F_n^l). The detailed mechanical behavior of the rolling resistance linear contact model is illustrated in Fig. 5. The symbols used are defined in Itasca (2020). The microscopic contact parameters that must be calibrated for this model include the friction coefficient (μ), effective modulus (E^*), rotation resistance coefficient (μ_r), normal critical damping ratio (β_n), and shear critical damping ratio (β_s).

For the simulation of conditioned soil in the discrete domain, the adhesive rolling resistance linear (ARRlinear) model is employed. Conditioned sandy cobble soil typically exhibits high plasticity and flowability, accompanied by low internal friction and cohesion. The ARRlinear model effectively captures the mechanical properties of such soils (Wan et al., 2025). The ARRlinear model is based on the rolling resistance linear model, incorporating a cohesive component. The cohesion of the cohesive rolling resistance linear model originates from short-range attractive forces, which are a linear approximation of van der Waals forces. The difference between short-range attractive forces and cohesive materials in PFC is that there is no concept of fracture; that is, as long as the interacting surfaces are within the specified range of attraction, the attraction always exists. The details and mechanical behavior of this model are shown in Fig. 6, with symbol explanations provided by Itasca (2020). The microscopic contact parameters that need to be calibrated for the bonded rolling resistance linear contact model include the friction coefficient (μ), effective modulus (E^*), rolling friction coefficient (μ_r), normal critical damping ratio (β_n), shear critical damping ratio (β_s), maximum attractive force (F_0), and attraction range (D_0).

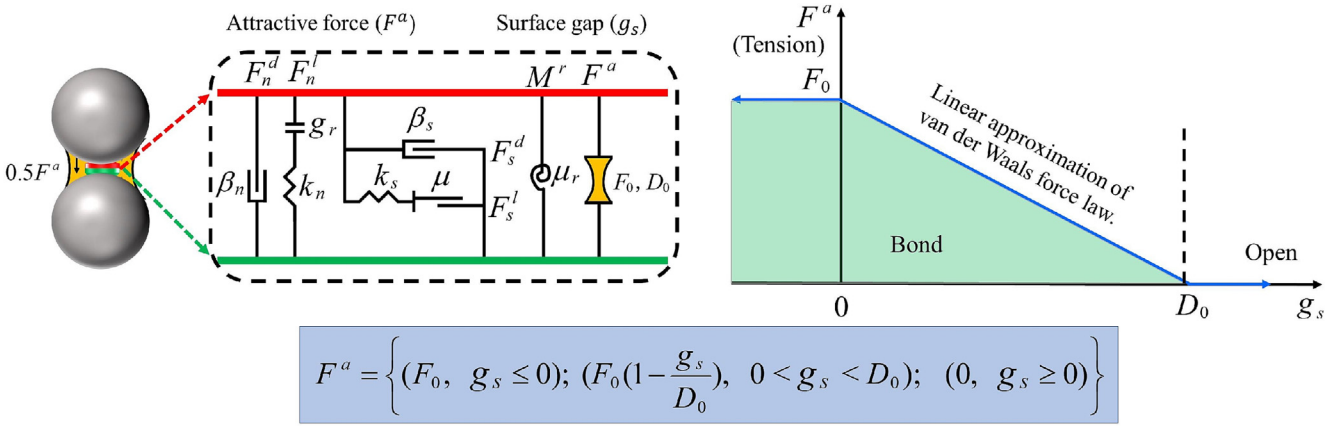

Fig. 6. Behavior and rheological components of the adhesive rolling resistance linear model.

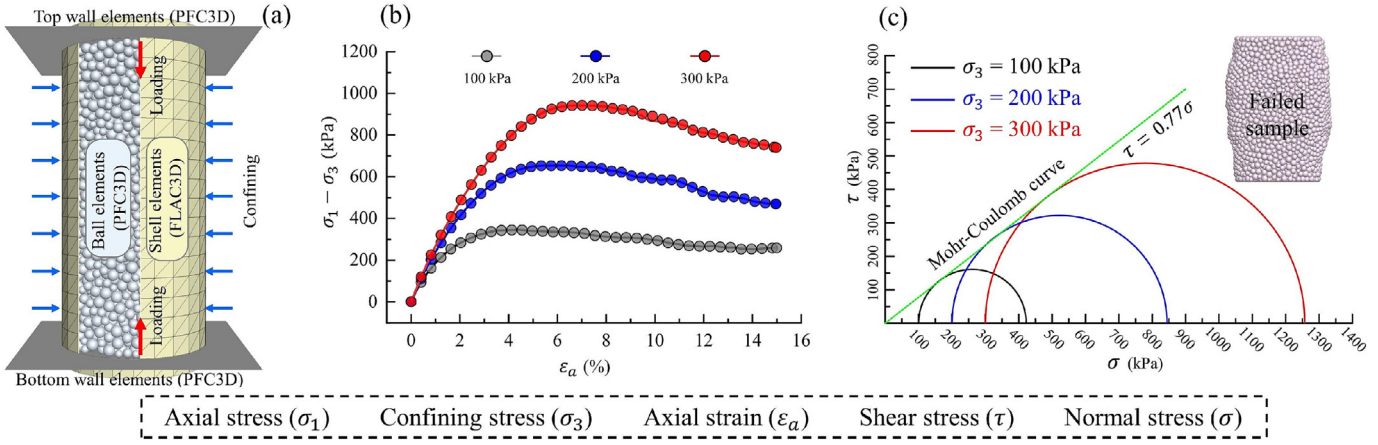

Fig. 7. Microscopic parameter calibration for the sandy cobble granular with $\varphi = 38°$. (a) Model of triaxial test sample, (b) stress–strain curves for a numerical triaxial test, and (c) Mohr–Coulomb criterion and Mohr's circle.

3.3 Soil material properties

In DEM simulations, the macroscopic mechanical behavior of soil is reproduced by calibrating its microscopic mechanical properties (Fakhimi et al., 2002). However, DEM simulations are computationally intensive, and the calculation time increases significantly with the number of particles in the discrete domain. To balance computational efficiency and accuracy, based on previous studies (Schöpfer et al., 2009), which suggest that the ratio of tunnel diameter to median particle size should not be less than 10, particles with a uniform size distribution ranging from 12 to 20 cm (d_{50} = 16 cm) were adopted in this study.

To calibrate the microscopic parameters of the undisturbed soil, numerical triaxial tests were conducted. As illustrated in Fig. 7(a), spherical elements in PFC3D were utilized to represent soil particles, while shell elements in FLAC3D were employed to simulate the rubber membrane. Based on previous research (H. X. Zhu et al., 2020), the rubber membrane was assigned an elastic modulus of 3.0 MPa, a thickness of 5 mm, and a density of 930 kg/m^3. The tests were performed under strain-controlled loading conditions, achieved by specifying the velocities of the top and bottom loading plates. A constant confining pressure (100, 200, and 300 kPa, corresponding to the tunnel burial depth) was applied to the rubber membrane to simulate lateral constraints. To ensure simulation accuracy, the specimen dimensions were set as a diameter (D) of 2.6 m and a height (H) of 5.2 m, with the friction coefficient between the specimen and the loading plates set to zero to replicate ideal conditions. As shown in Fig. 7(b) and (c), the numerical tests generated stress–strain curves and Mohr–Coulomb failure criterion curves for the undisturbed soil ($\varphi = 38°$). The slope of the latter was 0.77, corresponding to a simulated soil friction angle of 37.8°, which closely matches the in-situ friction angle of the undisturbed soil. This demonstrates that the particles in the DEM model effectively replicate the mechanical properties of the in-situ undisturbed soil. The parameters used in the numerical triaxial tests are detailed in Table 3.

Given that slump tests are widely employed to evaluate the effectiveness of soil conditioning in shield tunneling engineering (Vinai et al., 2008), this conventional method

Table 3
Details of triaxial test model for calibration of contact parameters of in-situ soil.

Property	Value
Dimension of specimen, D (m) × H (m)	2.6 × 5.2
Diameters of ball element (cm)	12–20
Density of ball element (kg/m^3)	3200
Porosity	0.353
Contact model	Rolling resistance linear
Thickness of shell element (mm)	5.0
Density of shell element (kg/m^3)	930
Elastic modulus of shell element (MPa)	3.0
Confining pressure (kPa)	100, 200, 300
Effective modulus, E^* (MN/m^2)	50
Stiffness ratio	1.5
Friction coefficient, μ	0.35
Rolling friction coefficient, μ_r	0.25
Normal critical damping ratio, β_n	0.2
Shear critical damping ratio, β_s	0.2

was replicated using the DEM. Slump tests were conducted to calibrate the microscopic parameters of the conditioned soil, as illustrated in Fig. 8. It is well established that the standard slump cone has a height (h) of 30 cm, with top and bottom diameters of 10 and 20 cm, respectively. According to ASTM C143/C143M standards (ASTM, 2015), a slump height-to-cone height ratio ranging from approximately 1/2–2/3 indicates suitable workability of the conditioned soil. However, due to the average particle size of 16 cm in the DEM model, conducting standard-sized slump tests was impractical. Therefore, based on recommendations from Schöpfer et al. (2009), the dimensions of the slump cone were scaled up by a factor of 20. To ensure the simulated conditioned soil met the required workability, the target slump height in the numerical model was set between 300 and 400 cm, corresponding to a ratio of 1/2–2/3 of the scaled cone height (600 cm), consistent with the standard test. As shown in Fig. 9, after adjusting the microscopic parameters, the simulated slump height of the conditioned sandy cobble soil was 380 cm. This result demonstrates that the selected microscopic parameters effectively replicate the macroscopic mechanical properties of the conditioned sandy cobble soil. Table 4 compares the slump parameters obtained from the numerical simulations with those specified by ASTM C143/C143M. Table 5 provides a detailed list of the mesoscopic parameters selected for the slump tests in this study.

3.4 Three-dimensional FDM–DEM coupled model

3.4.1 Ground modeling

The three-dimensional FDM–DEM coupled numerical model of the initial stratum is depicted in Fig. 10. To mitigate boundary effects, the overall model dimensions are set to 35 m in height, 30 m in width, and 12 m in length along the tunnel alignment. The discrete domain measures 10 m in height, 10 m in width, and 4 m in length along the tunnel alignment. Given that the initial stress field typically exhibits a gradient distribution with depth, it is essential to apply a reasonable gradient stress boundary condition within the discrete domain. However, conventional coupling methods (Liu et al., 2022) encounter difficulties in accurately simulating such depth-dependent stress gradients.

The FDM–DEM coupling method proposed by Liu et al. (2022) comprises the following key steps:

(1) Initial stratum model construction. The initial stratum model is established following the FDM (FLAC3D) modeling procedure.
(2) Overlapping region treatment. The region overlapping with the DEM discrete domain in the FDM model is removed, and a particle-based stratum model is generated within the DEM region.
(3) Stratum compaction simulation. The porosity of the particle assembly is adjusted to simulate the compaction state of the stratum until the settlement error falls within an acceptable range.

Despite achieving FDM–DEM coupling, this method presents practical challenges. The stress conditions in the discrete element region fail to satisfy the depth-dependent stress gradient, and inaccurate stress boundary conditions result in deviations in the internal stress distribution of the specimen from the actual scenario. To address these

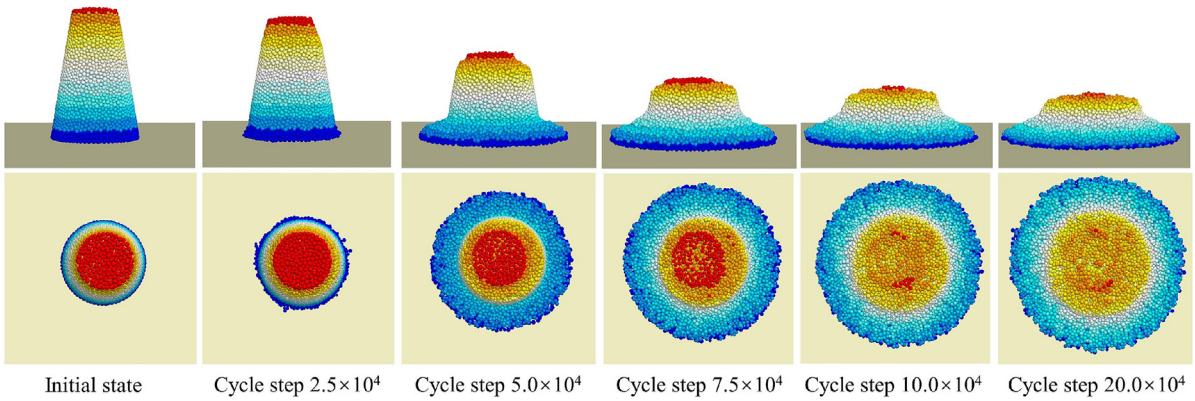

Fig. 8. Slump model of conditioned sandy cobble soil.

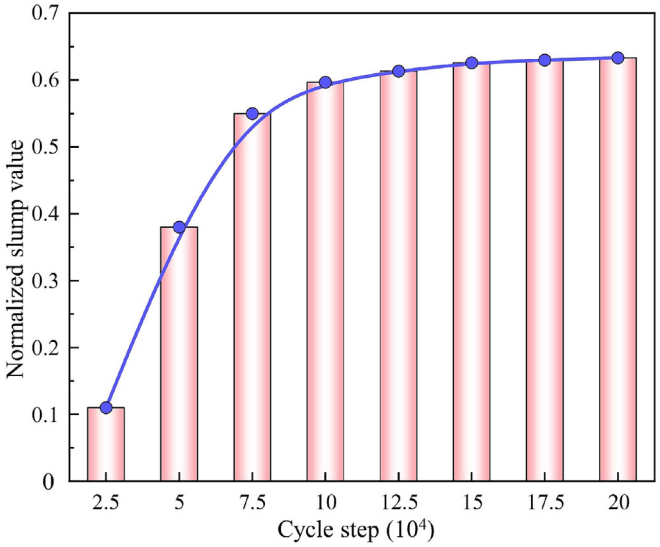

Fig. 9. Variation of slump with calculation steps.

Table 4
Comparison of slump values.

Project	Slump cone dimensions	Suggested slump values
Standard specification (ASTM C143/C143M)	10 cm × 20 cm × 30 cm	0.50*h*–0.66*h*
Numerical simulation	200 cm × 400 cm × 600 cm	0.63*h*

Table 5
Microscopic contact parameters of conditioned sandy cobble soil.

Property	Value
Effective modulus, E^* (MN/m^2)	5.0
Stiffness ratio	1.0
Friction coefficient, μ	0.25
Rolling friction coefficient, μ_r	0.15
Normal critical damping ratio, β_n	0.20
Shear critical damping ratio, β_s	0.20
Maximum attractive force, F_0 (N)	150
Attraction range, D_0 (mm)	0.10

limitations, this study proposes a novel gradient stress construction method based on rigid wall boundaries. This method enables precise simulation of stress gradients within the discrete domain through stepwise stress loading and a servo mechanism. The specific steps are as follows:

(1) Discrete domain and specimen generation. Six walls are generated based on the extent of the discrete domain in the model, and a particle specimen is created within the enclosed region of the walls.
(2) Isotropic stress state construction. Under the constraint of six rigid walls, horizontal stress is applied to the walls in the DEM region via the servo mechanism to achieve an isotropic stress state in the particle specimen (Fig. 11(a)). Notably, the target horizontal stress corresponds to the theoretical at-rest earth pressure at the center of the discrete domain.
(3) Vertical (z-direction) stress adjustment. Equal vertical stresses are applied to the top and bottom walls through the servo mechanism to place the particle specimen in an anisotropic stress state (Fig. 11(b)). It should be noted that the target vertical stress corresponds to the self-weight stress at the top of the discrete domain.
(4) Gravity field introduction. The displacement of the bottom wall (wall_1) is restricted, and its servo mechanism is removed. Gravity is applied to the model, and iterative calculations are performed until the system reaches equilibrium (Fig. 11(c)).
(5) Initial stratum model construction. Based on the overall model dimensions, the initial stratum model is established following the FDM (FLAC3D) modeling procedure. The overlapping region between the FDM model and the DEM discrete domain is removed. Wall_6 is retained while other walls are deleted. The FDM–DEM coupling command is activated, and coupling walls are generated to effectively link the two numerical methods. Iterative calculations are then performed until the system reaches equilibrium, resulting in a stable state of the initial stratum model (Fig. 11(d)).

Through this approach, the initial stress in the DEM model is effectively simulated and developed, ensuring stress continuity at the FDM–DEM coupling boundary. Figures 12 and 13 illustrate the stress distributions and variation curves under the FDM model, the traditional FDM–DEM coupling method, and the coupling strategy proposed in this study. Comparative analysis demonstrates that the stress results obtained from the proposed coupling strategy align closely with those from the FDM model or theoretical calculations, validating the effectiveness and reliability of the method.

3.4.2 EPB shield tunneling modeling

To enable precise numerical simulation of EPB shield tunneling, meticulous coupling and initialization of the shield machine and ground models are required. The following measures are implemented to ensure the accuracy and efficiency of the simulation.

First, to minimize disturbances to the initial ground stress distribution, the leading cutter of the cutterhead is positioned just to contact ground particles. This configuration prevents significant stress variations that could arise from fully embedding the shield machine, thereby preserving the accuracy and validity of the initial stress state. Moreover, initiating the simulation from this contact state eliminates the need to model gradual surface penetration, substantially reducing computational time and enhancing efficiency.

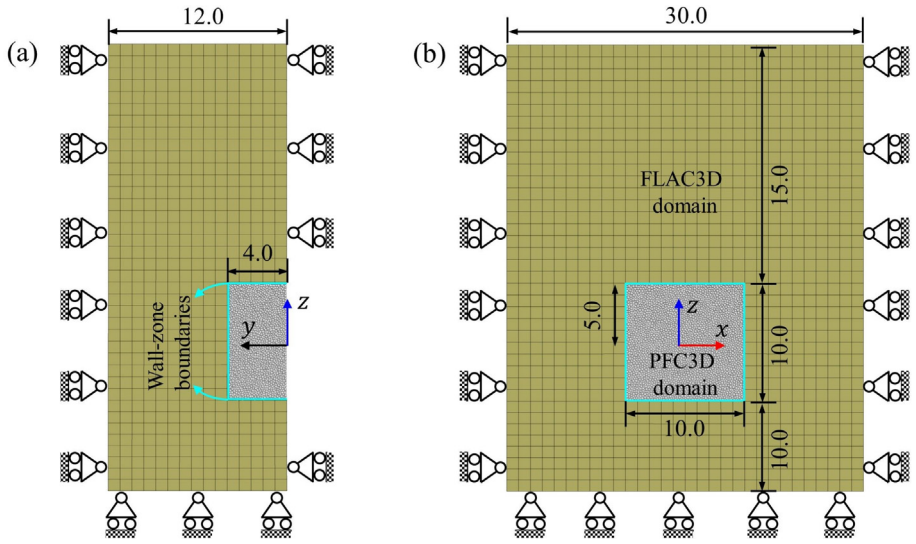

Fig. 10. Coupled FDM–DEM ground formation. (a) Cross-sectional view, and (b) front view. (Unit: m)

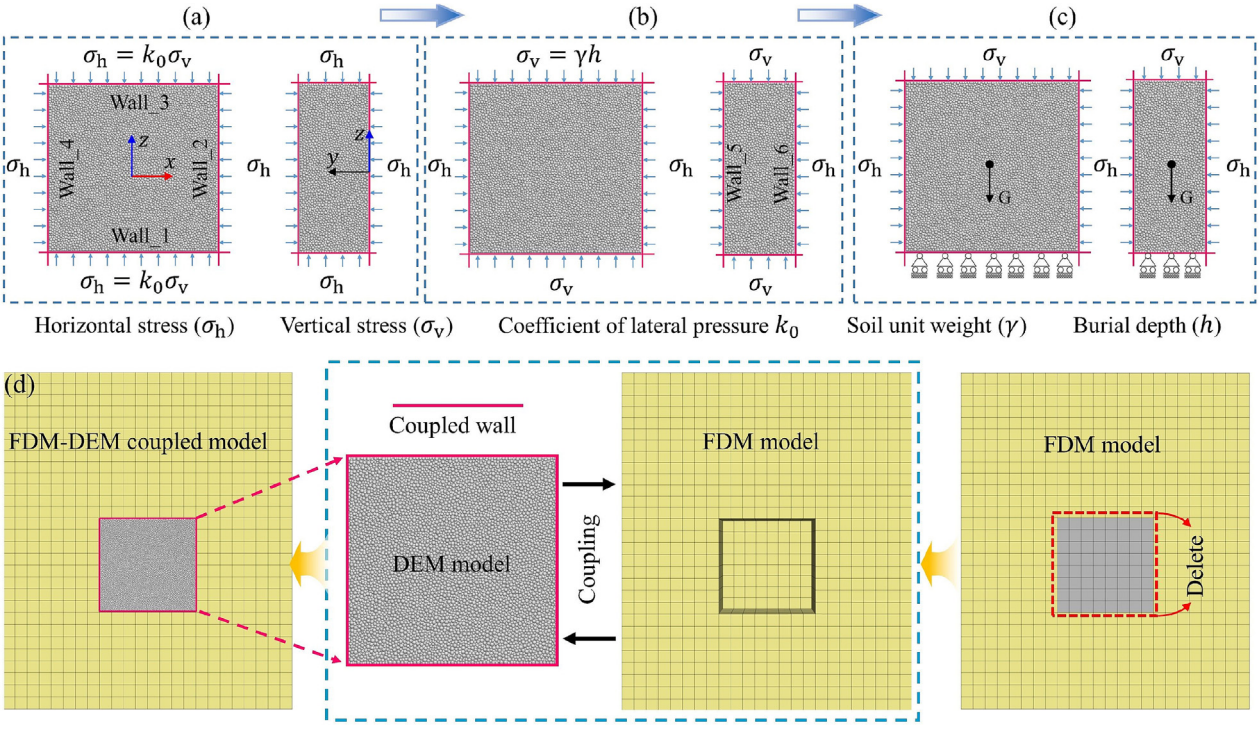

Fig. 11. Key steps for gradient stress implementation strategy. (a) Isotropic stress state, (b) vertical stress modification, (c) gravitational field introduction, and (d) FDM–DEM coupling.

Secondly, to prevent excessive surface settlement caused by the rapid influx of particles into the soil chamber during the early tunneling phase, sufficient particles are pre-filled in both the cutterhead region and the soil chamber to maintain a filled state. Excessive settlement could affect the contact at the FDM–DEM coupling boundary, leading to analysis failure. The pre-filling effectively mitigates this risk, ensuring stability during the initial tunneling phase.

Finally, to accurately reflect the mechanical behavior of conditioned soil, contact parameters of particles within a $D/30$ range ahead of the cutterhead and in the soil chamber are adjusted to match the properties of improved soil. Following initialization, equilibrium calculations are performed to achieve model stability, after which operational parameters are assigned to the shield machine model for subsequent tunneling simulation (Fig. 14).

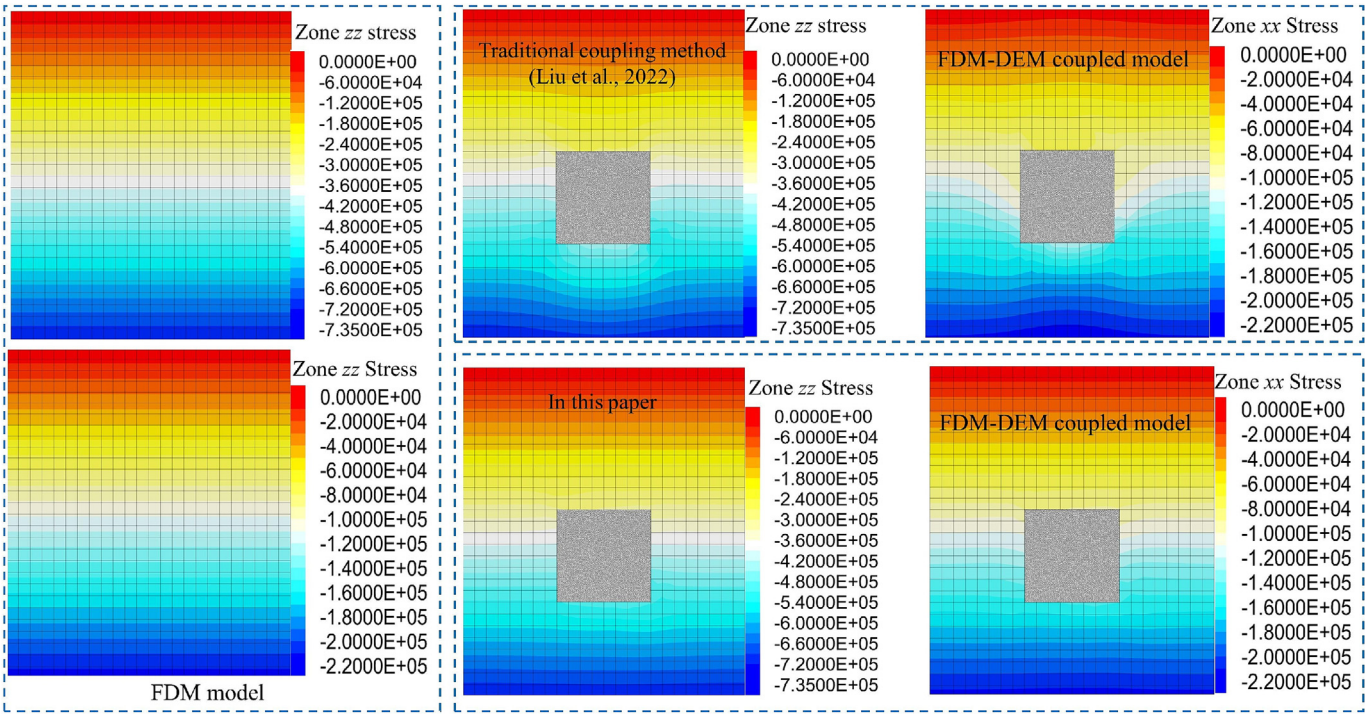

Fig. 12. Initial stress distribution patterns in different methods.

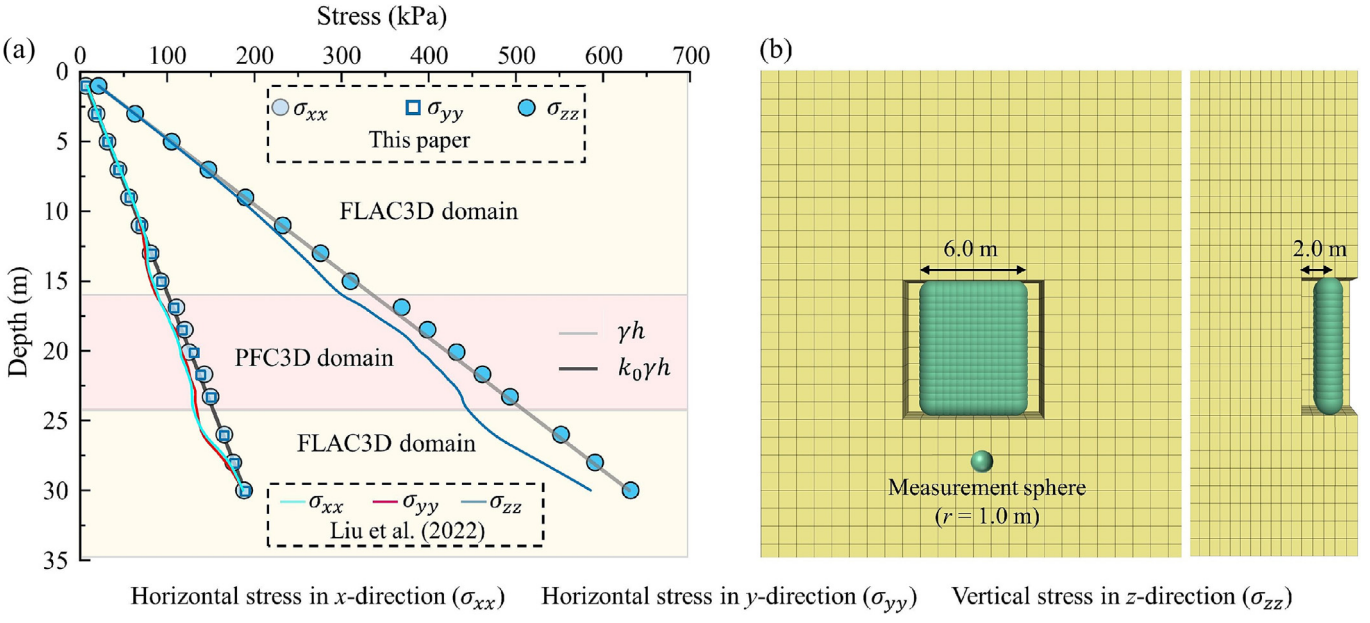

Fig. 13. Initial ground stress distribution and sensor layout in the coupled FDM–DEM model. (a) Initial ground stress distribution, and (b) DEM region sensor layout.

Under typical ground conditions, the actual rotation speed and advancement speed of the shield machine are 1 r/min and 60 mm/min, respectively. Directly applying these speeds in the DEM model for excavation simulations would result in an impractical model run time of several months. To address this issue, many studies accelerate the advancement speed to reduce computational time (Li et al., 2022). For example, Wu et al. (2020) conducted a sensitivity analysis of various advancement speeds to identify the optimal speed range for simulation. The results indicated that when the advancement speed is 10–150 times the actual excavation speed, the displacement results

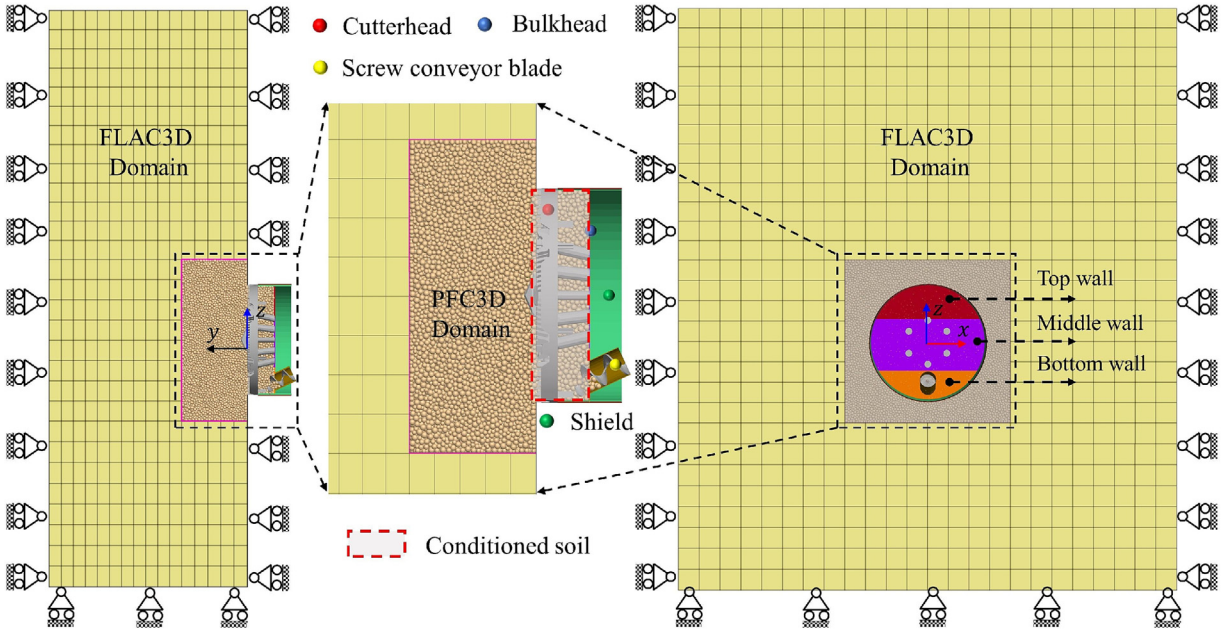

Fig. 14. Global and detailed views of the installed shield machine configuration.

remain largely consistent. Therefore, this study sets the advancement speed to 10 times the actual speed, striking a balance between computational efficiency and simulation accuracy. Specifically, in this numerical study, the shield advancement speed is set as 10 mm/s, with corresponding cutterhead and screw conveyor speeds of 6 and 35 r/min, respectively.

3.5 Verification of the rationality of the shield tunneling model

During EPB shield tunneling, to maintain face stability and control ground deformation, the volume of soil excavated by the cutterhead per unit time should equal the volume of muck discharged by the screw conveyor. The soil excavation volume is controlled by the shield advance speed ($Q_{in} = 0.25\pi D_c^2 v$, where D_c denotes the external diameter of the cutterhead, $D_c = 6600$ mm, Q_{in} is the soil excavation volume, and v is tunneling speed), while the muck discharge volume is regulated by the screw conveyor's rotational speed ($Q_{out} = 0.25\pi D_s^2 LN$, where Q_{out} is the muck discharge volume, D_s denotes the inner diameter of screw conveyor, L denotes screw pitch, and N denotes revolving speed of screw blade). As for the adopted shield machine, the values of those variables are as follows: $D_s = 800$ mm, $L = 800$ mm, and $N = 35$ r/min. A comparison between the numerical simulation results and theoretical values for the inflow and outflow volumes is shown in Fig. 15. As illustrated, the soil excavation volume (Q_{in}) and the muck discharge volume (Q_{out}) during shield tunneling are approximately equal, with a ratio of about 1.055. This indicates that the numerical model achieves a dynamic equilibrium state during shield tunneling.

The chamber pressure and cutterhead torque are critical monitoring parameters during EPB shield tunneling, as their variations reflect the stability of the shield advancement and directly influence face stability. The changes in chamber pressure (at the top wall position, see Fig. 14) and cutterhead torque during shield tunneling are illustrated in Fig. 16. As shown in Fig. 16(a), the chamber pressure exhibits minor fluctuations, and the cutterhead torque changes smoothly during the simulated shield tunneling process, indicating a dynamic equilibrium state. Notably, the average cutterhead torque obtained from the simulation falls within the reasonable range calculated by the empirical formula ($T = \alpha D_c^3$, T is the cutterhead torque), and in sandy cobble strata, the value of α ranges from 15 to 23) (Shi et al., 2011), further validating the rationality and reliability of the numerical model in this study. From Fig. 16(b), it can be observed that the cutterhead torque and chamber pressure during shield tunneling approximately follow a normal distribution, with a significant correlation between them. The cutterhead torque increases with the rise in chamber pressure.

To validate the effectiveness of the dynamic equilibrium mode in the numerical model during shield tunneling, systematic monitoring and analysis of the ground displacement field were conducted (as shown in Figs. 17 and 18, where S denotes the tunneling distance). Figure 17 illustrates the contour of vertical ground displacement during shield tunneling. To enhance the visualization of the displacement contour, particles within 1.2 times the cutterhead diameter were hidden during the post-processing stage. It is important to note that this treatment was applied only for graphical representation, and no particles were removed during the actual simulation. From the

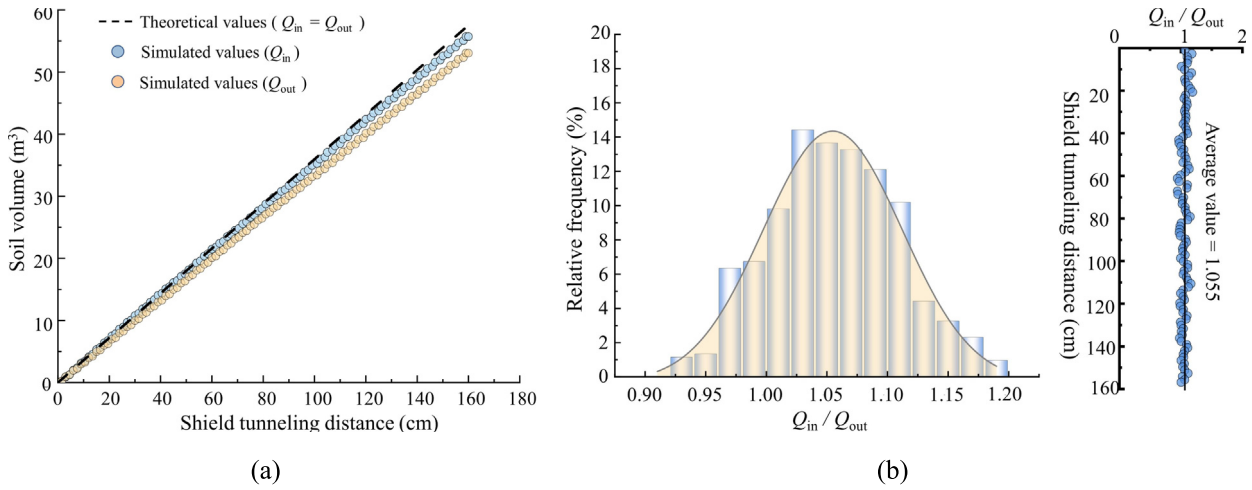

Fig. 15. Variation of in and out soil volumes during the shield tunneling process. (a) Changes in in/out soil volume with shield tunneling distance, and (b) relationship between in and out soil volumes.

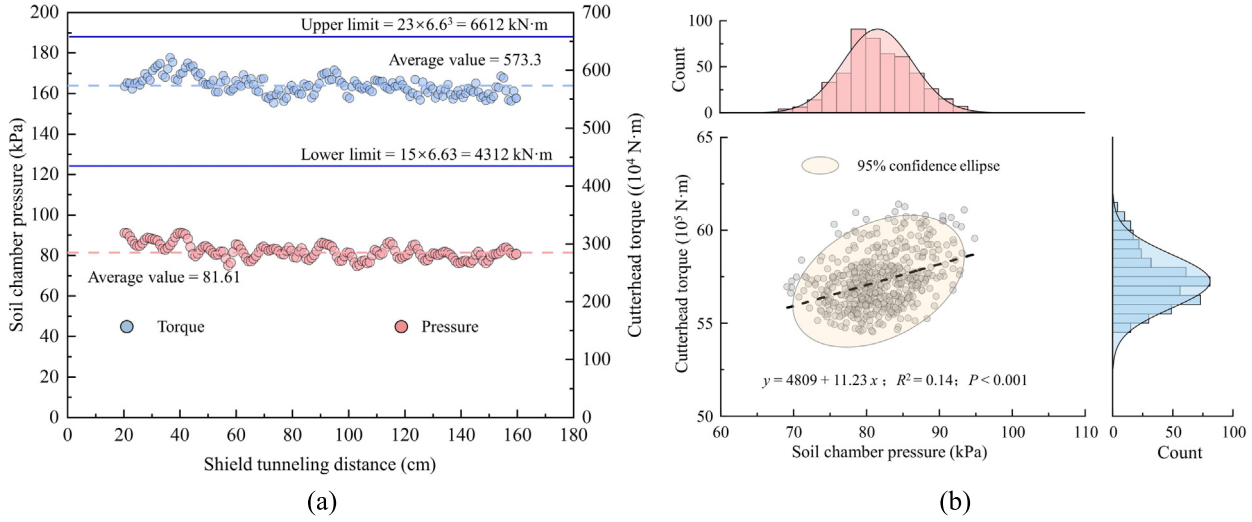

Fig. 16. Variation of chamber pressure and cutterhead torque during the shield tunneling process. (a) Changes in cutterhead torque and upper chamber pressure with shield tunneling distance, and (b) relationship and distribution of cutterhead torque and upper chamber pressure.

displacement field distribution in Fig. 17, it can be observed that the displacement values at the coupling boundary between the FDM and DEM regions exhibit high consistency, indicating that the coupling boundary maintains excellent displacement continuity during the calculation process. This result effectively validates the accuracy of the coupled calculation method.

Figure 18 presents the vertical ground surface displacement curve at the cross-section of $y = 2.0$ m during shield tunneling. The monitoring data reveal that the maximum vertical ground surface displacement increases with the tunneling distance and eventually stabilizes, reaching a maximum settlement of approximately 11.2 mm. This value falls within the reasonable settlement range (10–40 mm) specified in the Standard for Design of Shield Tunnel Engineering (GB/T 51438—2021) (Ministry of Housing and Urban-Rural Development of the People's Republic of China, 2021), indicating that ground surface settlement is effectively controlled throughout the tunneling process. Such control not only reflects the rationality of the EPB shield tunneling parameters but also demonstrates the maintenance of a dynamic equilibrium state during tunneling.

4 Results and analysis

4.1 Force transmission characteristics of sandy cobble granules

To systematically investigate the distribution characteristics of chamber pressure and the force transmission properties of muck during EPB shield tunneling in sandy cobble strata, a series of measurement spheres was deployed in the numerical model, as illustrated in Figs. 19 and 20.

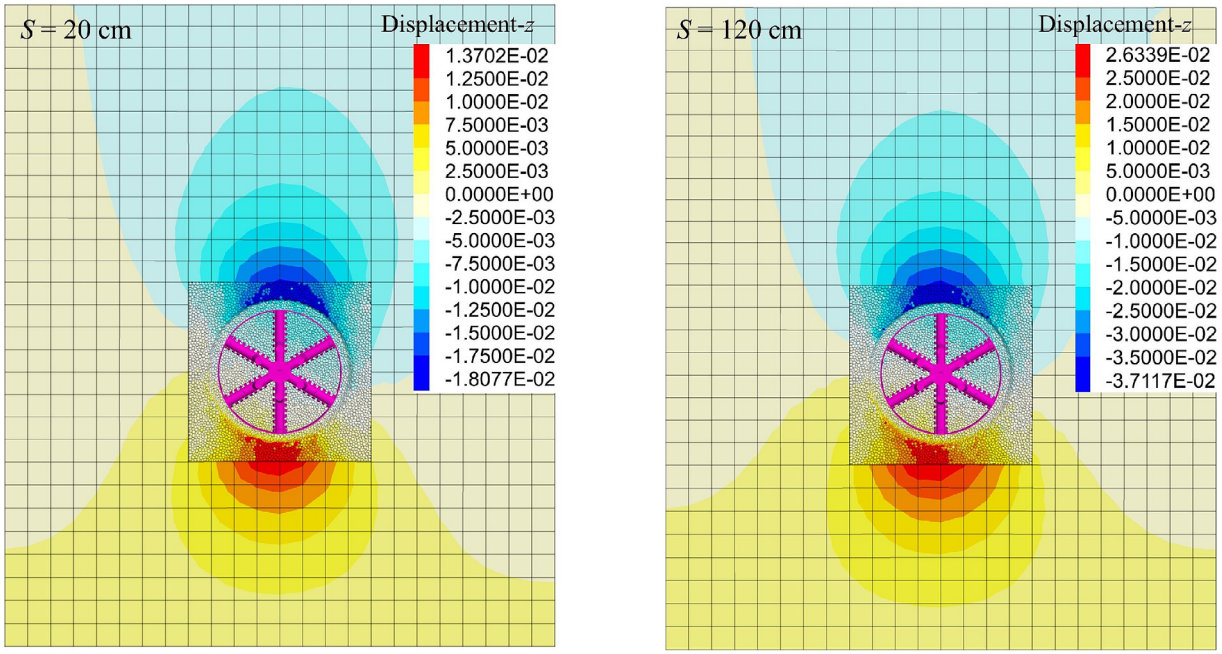

Fig. 17. Variation of vertical ground displacement contours during the shield tunneling process.

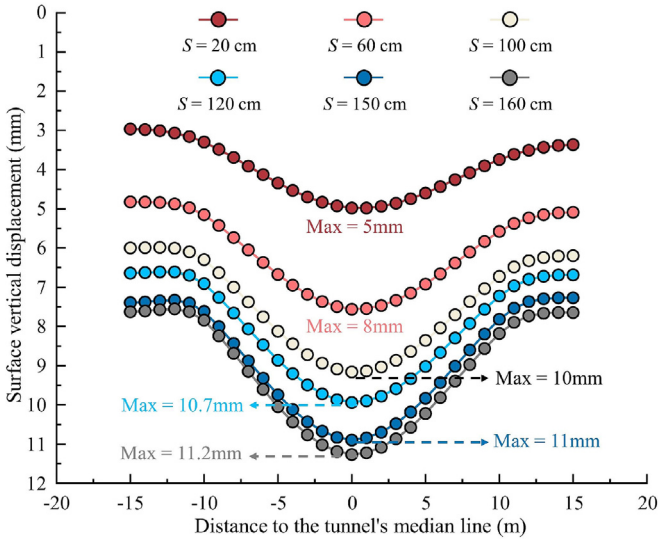

Fig. 18. Variation curve of surface vertical displacement during the shield tunneling process.

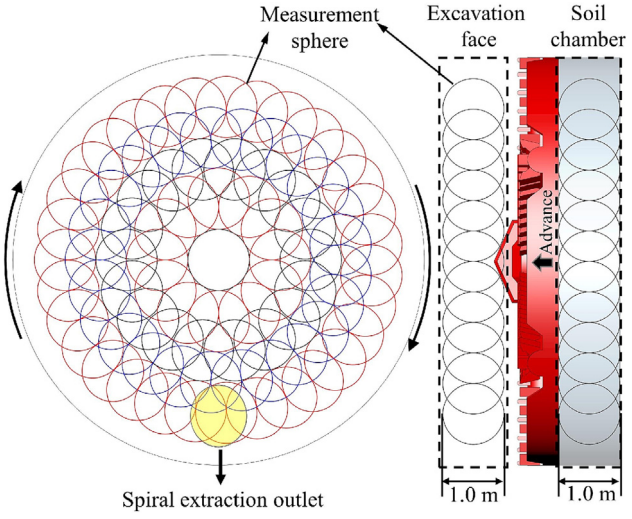

Fig. 19. Cutterhead front and soil chamber full section soil pressure monitoring point layout.

Figure 21 illustrates the distribution patterns of soil chamber and excavation face pressures at different tunneling distances during shield tunneling. As shown in the figure, both the excavation face and chamber pressures exhibit significant nonlinear characteristics. Specifically, at the excavation face, the pressure at the cutterhead ribs is relatively low, while the pressure at the opening is higher.

Within the soil chamber, the soil pressure shows a pronounced radial gradient, particularly near the bottom close to the screw conveyor entrance. Additionally, the direction of cutterhead rotation influences the pressure distribution within the soil chamber, resulting in asymmetric pressures on the left and right sides, with the pressure on the left typically lower than that on the right. This pressure imbalance is closely related to the rotation direction of the cutterhead, which further influences the pressure distribution within the soil chamber.

Figure 22 illustrates the pressure distribution at various measurement points within the excavation chamber. As shown in the figure, the muck pressure distribution on the left and right sides of the chamber exhibits significant asymmetry, primarily influenced by the rotational direction of the cutterhead. In this study, the cutterhead rotates clockwise along the tunneling direction during shield advancement, and its rotational action drives the muck toward the right side of the chamber, resulting in generally

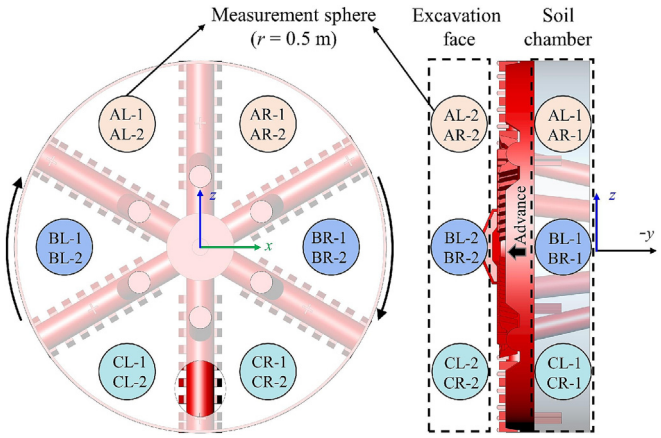

Fig. 20. Soil pressure monitoring point layout in specific regions.

higher pressure on the right side compared to the left. In the upper regions of both the left and right sides (i.e., at measurement points AL-1 and AR-1), the average pressure values are nearly equal, indicating a relatively uniform pressure distribution in the upper part of the chamber. The pressure values in this region can serve as a key reference for pressure control during shield tunneling.

Figure 23 presents the pressure distribution at various measurement points on the excavation face. By comparing the pressures on the left and right sides of the excavation face, the pressure variation characteristics during the shield tunneling process can be further analyzed. As shown in the figure, the pressure distribution on both sides of the excavation face is asymmetric. The pressures on the left side (AL-2, BL-2, and CL-2) and right side (AR-2, BR-2, and CR-2) increase gradually from top to bottom, with the pressure on the right side generally higher than that on the left. This asymmetry is primarily attributed to the rotation direction of the shield cutterhead. In the upper regions of both sides of the excavation face, specifically at the AL-2 and AR-2 monitoring points, the average pressures are nearly equal.

In engineering practice, the chamber pressure is typically set based on empirical methods, with the common assumption that the bulkhead pressure equals the face pressure. However, this study reveals that when an EPB shield operates in a dynamic equilibrium state, the chamber pressure does not equal the face pressure, which aligns with the findings of Hu et al. (2022). This discrepancy primarily arises from the pressure transmission losses during the motion of muck within the chamber.

Figure 24 illustrates the variation in the muck pressure transmission coefficient (the ratio of muck pressure inside the chamber to the face pressure) at different measurement points. The results show that the average pressure transmission coefficients in regions AL and AR are both 0.81, indicating uniformity in the pressure transmission coefficients on both the left and right sides of the upper chamber and confirming the homogeneous distribution of muck pressure in this region. However, significant differences exist in the pressure transmission coefficients between the

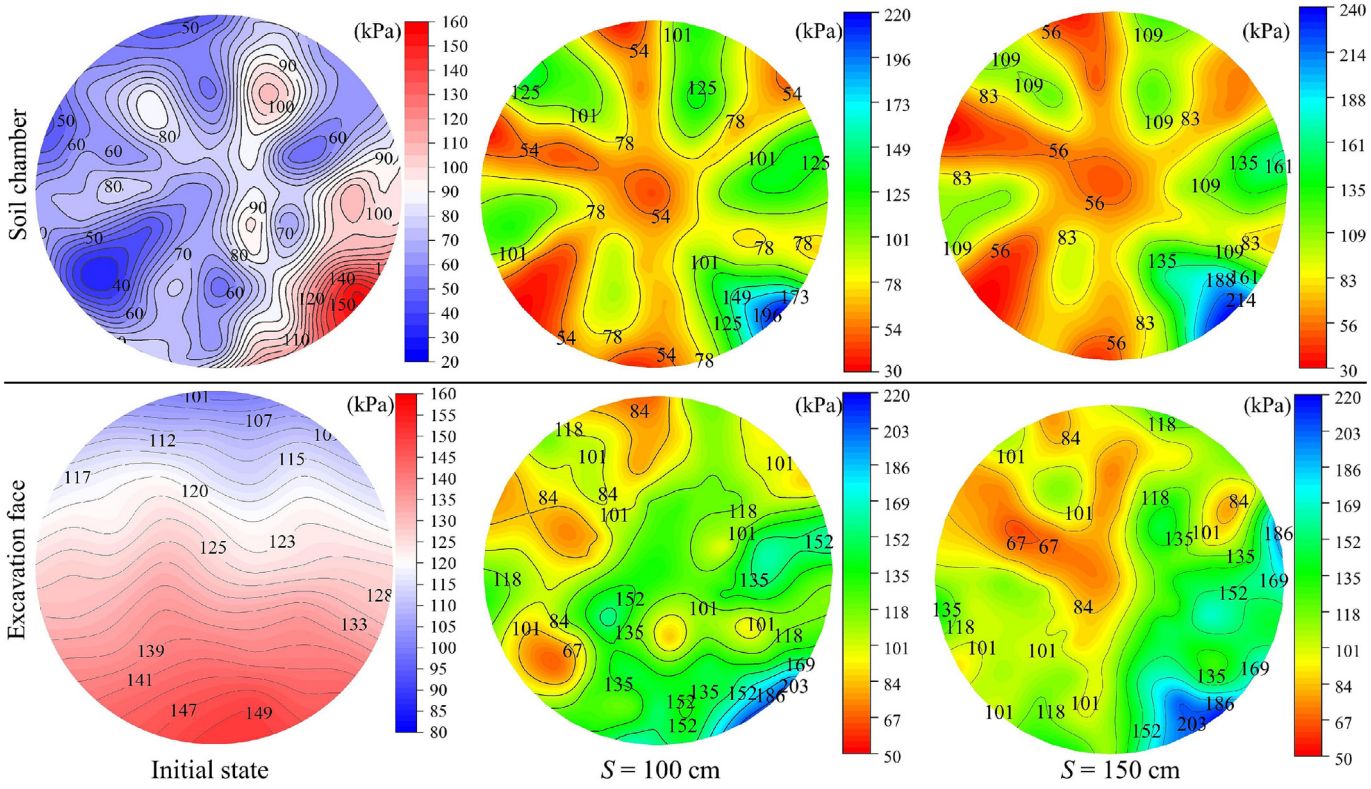

Fig. 21. Distribution of soil chamber and excavation face pressures.

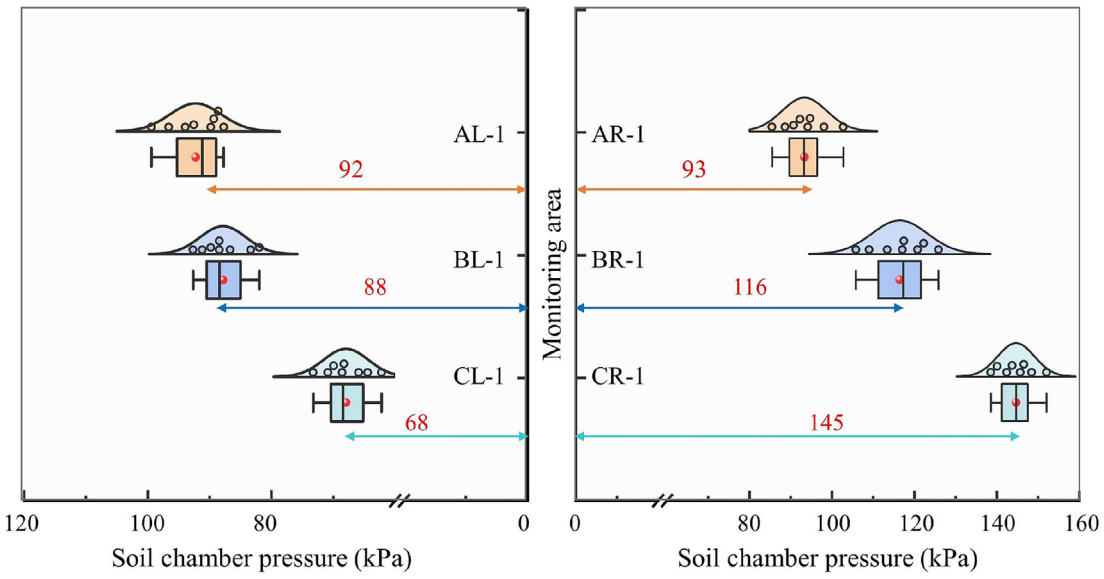

Fig. 22. Pressure distribution at various measurement points within the soil chamber.

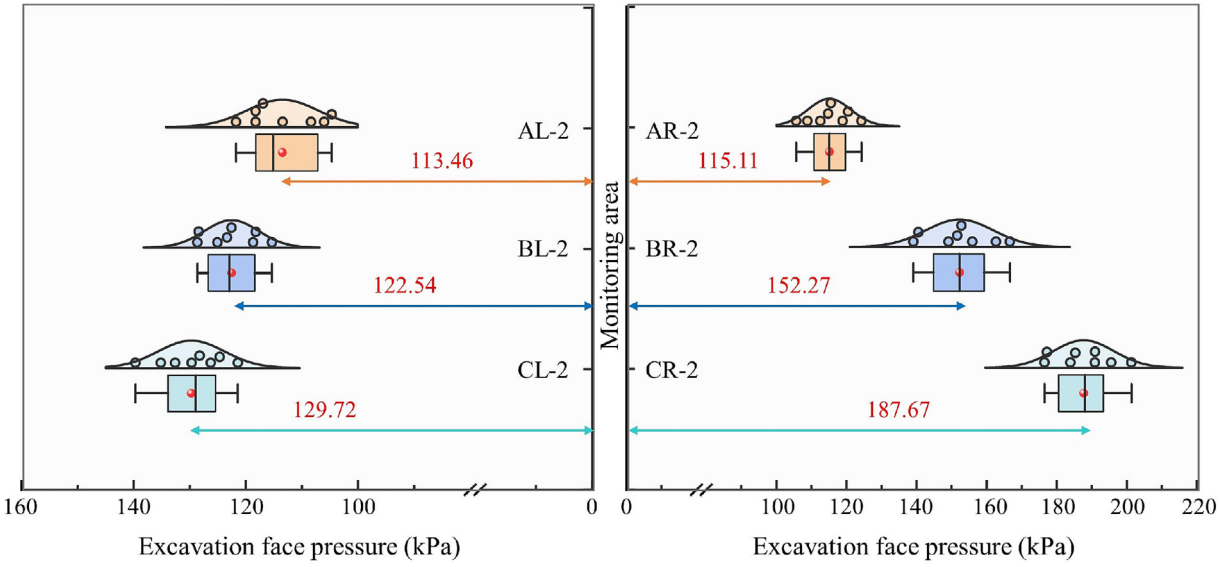

Fig. 23. Pressure distribution at various measurement points on the excavation face.

left and right sides in the middle and lower regions of the chamber, with the right side exhibiting notably higher values. This difference is primarily attributed to the stronger compaction effect on one side of the chamber caused by cutterhead rotation, resulting in significant pressure variations.

4.2 Motion patterns of sandy cobble granules

During EPB shield tunneling, identifying localized muck stagnation zones in front of the cutterhead and within the chamber can provide a scientific basis for optimizing tunneling parameters and cutterhead design, thereby ensuring safe and efficient construction. Based on the structural characteristics of the cutterhead, a large number of tracer particles were systematically distributed in different regions in front of the cutterhead to comprehensively capture and analyze the spatial transport patterns of muck particles during shield tunneling. The specific arrangement of tracer particles is detailed in Fig. 25, with their initial distance from the cutterhead central axis denoted as R.

4.2.1 Motion trajectories of sandy cobble granules

Figure 26 illustrates the motion trajectories of tracer particles at different locations during the 160 cm advancement of the EPB shield. The results indicate that, under the combined effects of gravity, contact forces, and centrifugal forces, tracer particles at different locations exhibit

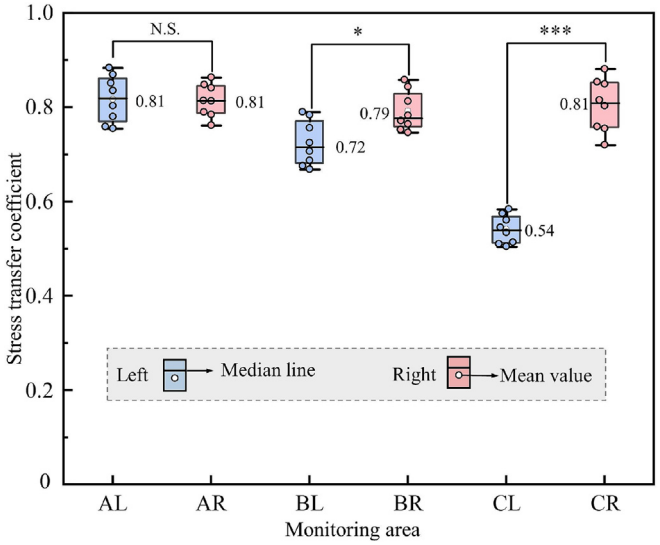

Fig. 24. Variation of soil pressure transmission coefficient.

distinct motion patterns. Overall, all tracer particles display pronounced spiral trajectories. Further analysis reveals that the radial motion of tracer particles can be categorized into two primary modes: (1) Gradual deviation from their initial radial positions, as observed in tracer particles a1–a6, b1–b5, c1–c6, and d1–d6. These particles are typically located within a radial range of 0–2.3 m from the cutterhead, where muck particles, subjected to cutterhead cutting and extrusion, move away from their initial positions and disperse outward. (2) Maintenance of their initial radial positions, as seen in tracer particles e1–e6. The axial motion paths of tracer particles can also be divided into two scenarios: (1) Trajectories of tracer particles completing the process from the excavation face to the chamber, such as tracer particles a1–a6, b1, b5, and c3. These particles exhibit longer retention times within the chamber and smaller axial displacement ranges. (2) Trajectories of tracer particles completing the entire transport process from the excavation face to the chamber and then to the screw conveyor. These particles have shorter retention times within the chamber and larger axial displacement ranges.

Figure 27 illustrates the variation in the axial positions of tracer particles during shield tunneling. Analysis reveals that in the initial stage of cutterhead excavation at the tunnel face, tracer particles primarily undergo small but intense reciprocating motions in front of the cutterhead. As the shield machine advances, tracer particles gradually enter the chamber through the cutterhead openings and are eventually discharged. During this stage, the axial displacement of particles shows a distinct stepwise increase, indicating that once particles enter the chamber, they rapidly move toward the outlet under the disturbance of the cutterhead and mixing rods, with the reciprocating motion diminishing accordingly. Notably, due to soil conditioning, the motion of muck particles within the chamber exhibits higher stability and consistency.

The residence time of muck particles at different locations on the tunnel face varies significantly in front of the cutterhead and within the chamber. Tracer particles located within the width range of the fishtail tools (a1–a6) experience prolonged retention in front of the cutterhead due to the zero opening ratio in this region, and none are discharged from the chamber. In contrast, particles near the outer edge of the cutterhead (e1–e6), benefiting from a higher opening ratio that provides sufficient space to respond to cutting disturbances, exhibit shorter reten-

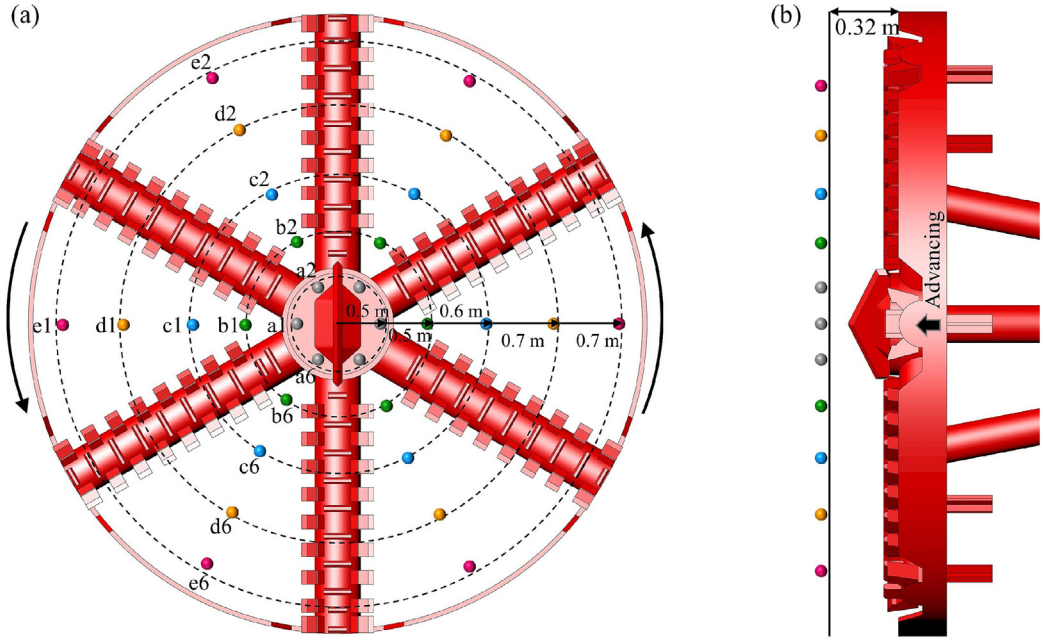

Fig. 25. Schematic diagram of tracer granule layout. (a) Front view, and (b) side view.

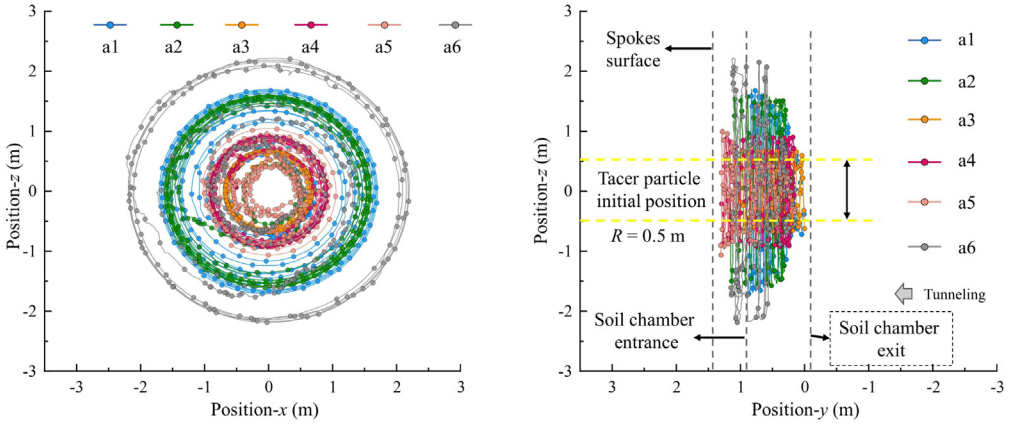

(a)

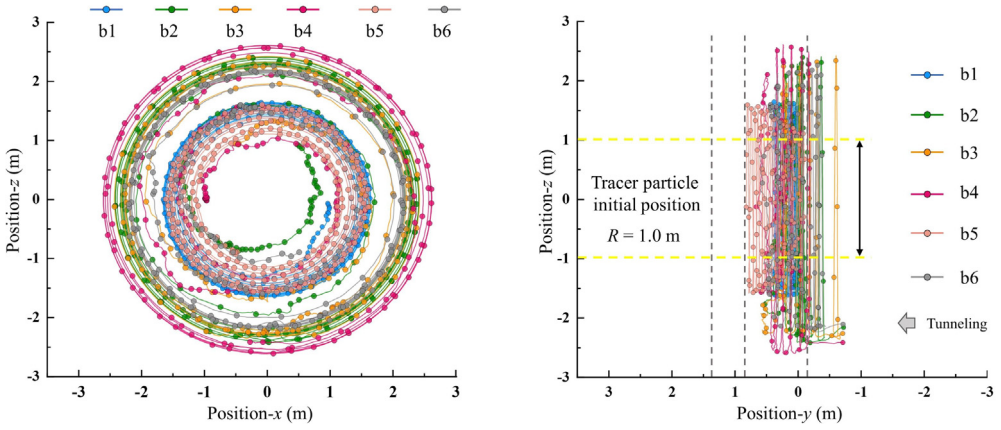

(b)

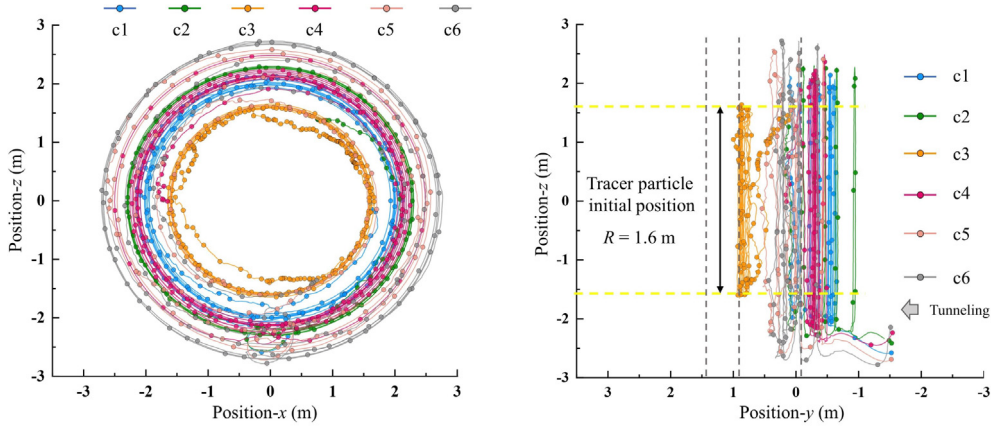

(c)

Fig. 26. Tracer granule trajectories during 160 cm shield advancement. (a) Trajectories of tracer granules a1–a6, (b) trajectories of tracer granules b1–b6, (c) trajectories of tracer granules c1–c6, (d) trajectories of tracer granules d1–d6, and (e) trajectories of tracer granules e1–e6.

tion times in front of the cutterhead and are all successfully discharged. In this region, the axial displacement of muck particles increases significantly, ensuring rapid entry into the chamber and smooth discharge.

4.2.2 Motion velocity of sandy cobble granules

Figures 28 and 29 illustrate the motion characteristics of muck particles during shield tunneling. The particle velocity in front of the cutterhead exhibits significant non-

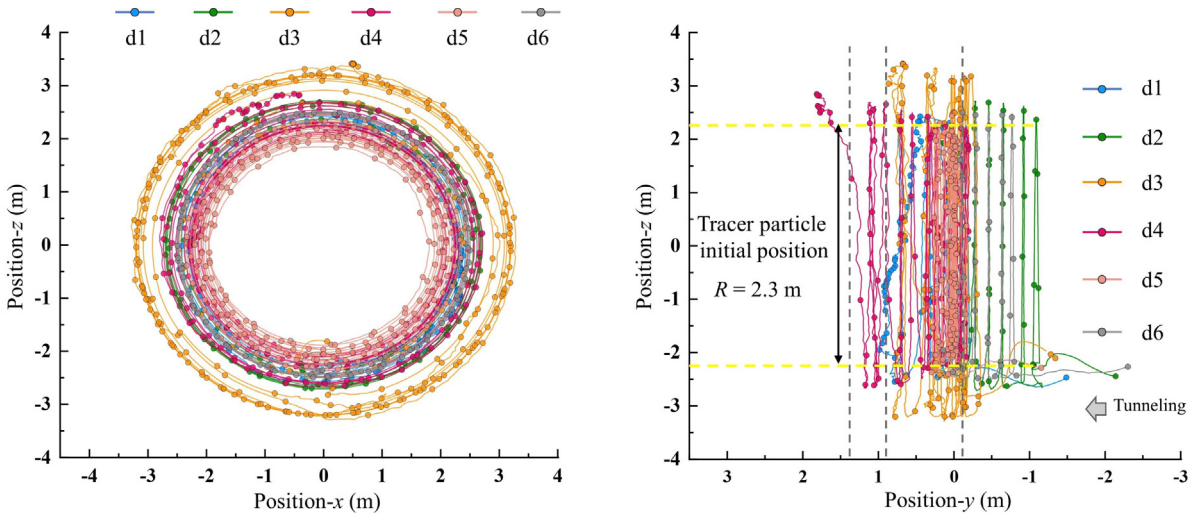

(d)

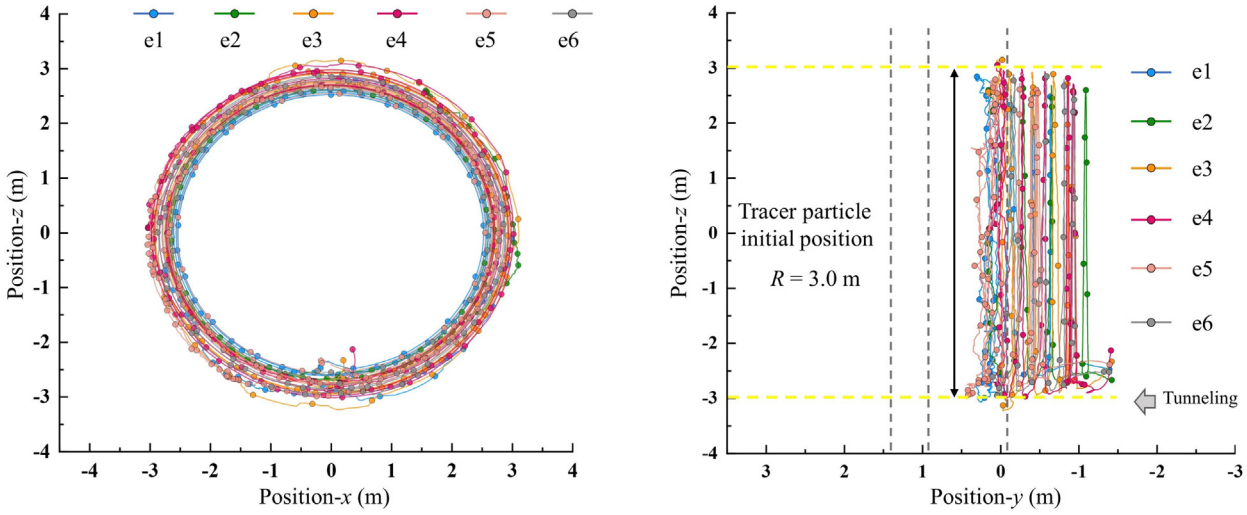

(e)

Fig 26. *(continued)*

uniformity, increasing from the center outward, reflecting the complex disturbance patterns generated by the cutterhead rotation through shear and extrusion. The velocity fields at the chamber entrance and middle regions are relatively uniform, indicating that particles stabilize after high-speed movement through the entrance, although the velocity still increases from the center outward. Statistical analysis of average velocities shows that the velocities at the chamber entrance and middle regions are nearly equal, while the velocity in front of the cutterhead is the lowest. The analysis reveals that the regions in front of the cutterhead and at the center of the chamber are the primary muck stagnation zones, with low particle migration velocities. To address this issue, the tool arrangement or muck discharge channels in the central region of the cutterhead should be improved to enhance particle velocities in this area. Additionally, the internal structure of the chamber should be optimized to guide effective muck flow and avoid low-velocity stagnation in the central region.

4.2.3 Spatial distribution of sandy cobble granules

Figure 30 reveals the spatial distribution characteristics of soil particles entering the chamber under cutterhead cutting during shield tunneling. It can be observed that muck particles entering the chamber are predominantly concentrated in the peripheral regions ($1.3 < R' < 3.3$, where R' denotes the radial distance from the chamber center), with a significantly higher mass proportion compared to the central region ($R' < 1.3$). The high mobility of muck in the peripheral regions, characterized by elevated particle

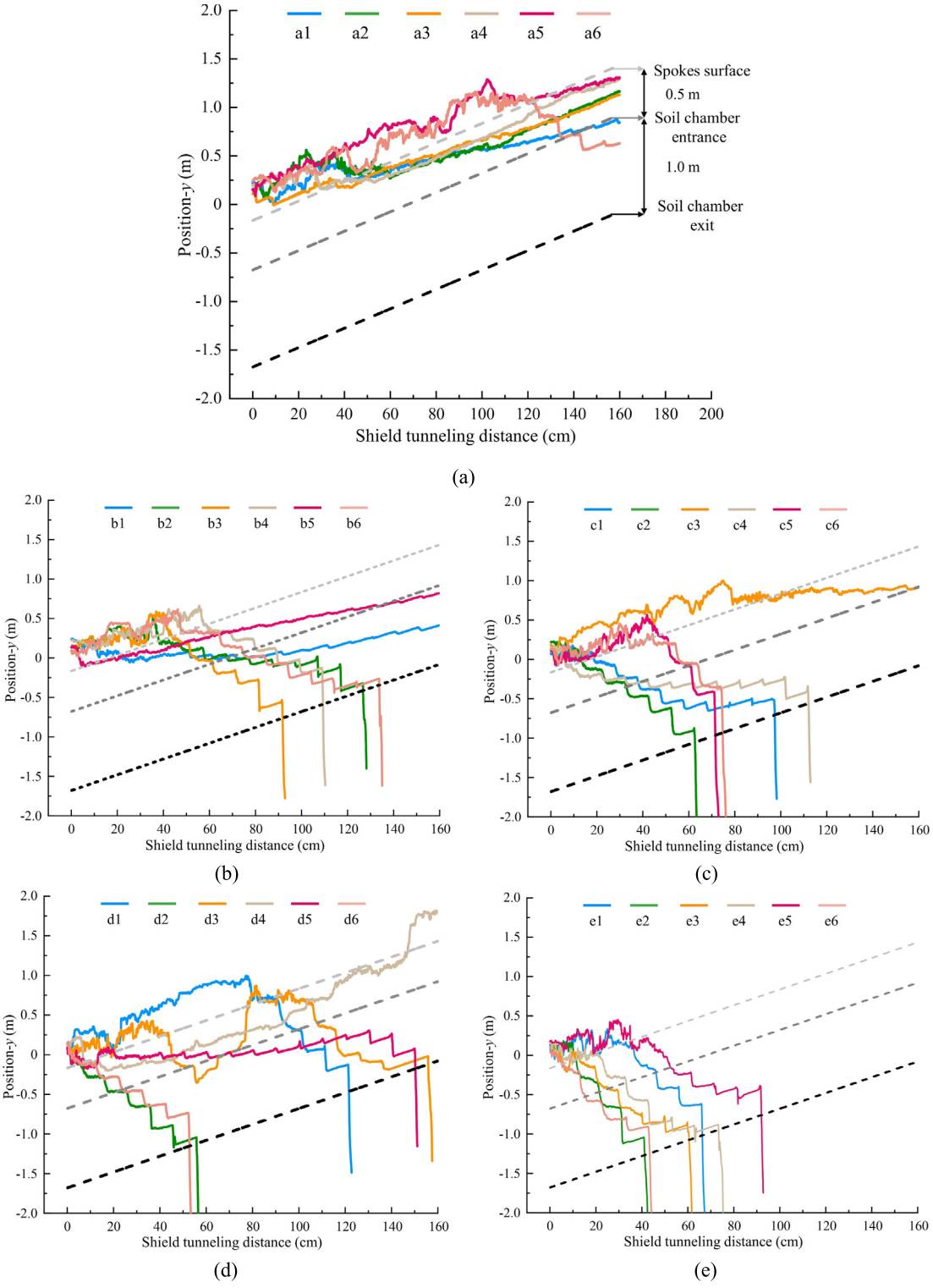

Fig. 27. Axial displacement patterns of tracer granules during shield tunneling advancement. (a) Axial displacement of tracer granules a1–a6, (b) axial displacement of tracer granules b1–b6, (c) axial displacement of tracer granules c1–c6, (d) axial displacement of tracer granules d1–d6, and (e) axial displacement of tracer granules e1–e6.

migration rates, is attributed to the intense shear field (dominated by cutterhead rotational energy) that suppresses particle agglomeration and stagnation. In contrast, the central region exhibits localized particle accumulation due to energy gradient attenuation, where particles are prone to frictional resistance and gravitational effects.

Figure 31 displays the variation in muck retention rates across different zones in front of the cutterhead. The data

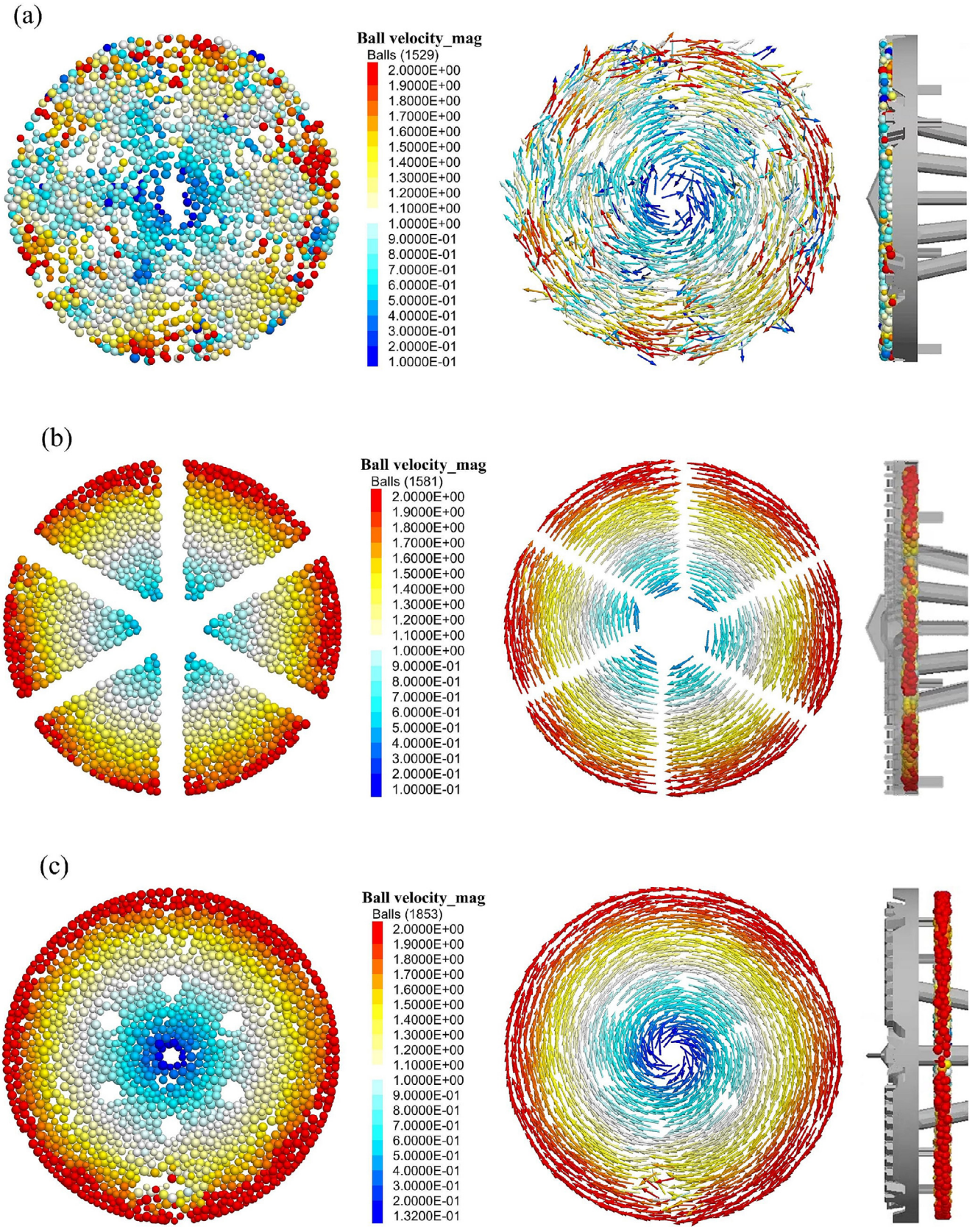

Fig. 28. Velocity contours and velocity field distribution of soil granules. (a) Ahead of the cutterhead, (b) near the entrance of the soil chamber, and (c) in the middle of the soil chamber.

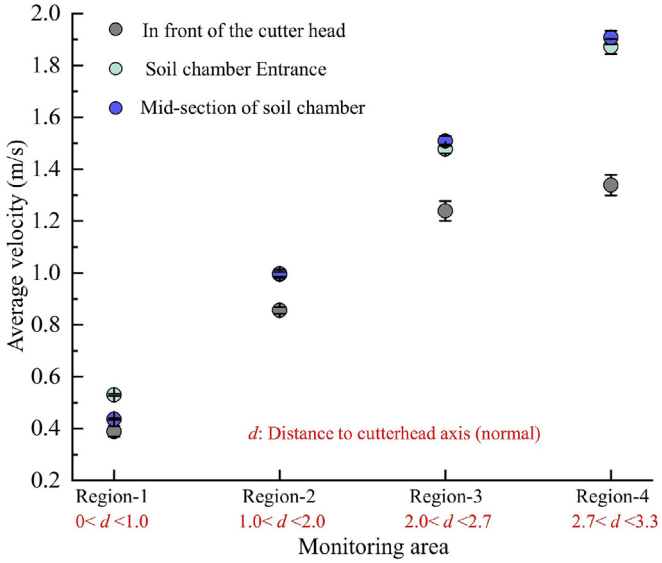

Fig. 29. Average soil granule velocity variation.

indicate a relatively high retention rate in Area-1, primarily caused by its central location on the cutterhead and the lower local opening ratio. As the monitored zones gradually move away from the cutterhead center, the local opening ratio increases, leading to a progressive reduction in retention rates and shorter retention times in front of the cutterhead, particularly in Area-5.

Figure 32 illustrates the volumetric changes of muck particles entering the chamber from different zones in front of the cutterhead. The results show that Area-1 has a smaller volume proportion, consistent with the higher retention rate observed in Fig. 31, further confirming the susceptibility of these regions to muck stagnation. As tunneling progresses, the volume proportions of muck particles entering the chamber from all zones stabilize.

Figure 33 illustrates the variation pattern of soil granule volume distribution entering the soil chamber from the excavation face during shield tunneling. Figure 34 shows the distribution of soil granules within the soil chamber when the shield has advanced to 150 cm. Based on the data analysis of Fig. 33, it is observed that the volume share of soil granules entering the soil chamber gradually increases with the excavation distance, reaching saturation at approximately 120 cm. The growth curve of granule volume distribution exhibits a typical nonlinear characteristic, indicating a gradual accumulation effect in the filling of soil granules. The volume of granules within the soil chamber stabilizes after a certain excavation distance.

Figure 34 further details the granule distribution within the soil chamber, highlighting a distinct layered characteristic. The region near the center of the soil chamber contains existing soil granules, while the outer region is populated by soil granules entering from the excavation face. This distribution pattern is closely linked to the cutterhead opening characteristics and the mixing devices within the soil chamber. Specifically, soil granules from the excavation face, under the cutting and disturbance effects of the cutterhead, are mainly distributed in the region approximately 0.25D–0.50D from the center of the soil chamber. In contrast, the region closer to the center of the soil chamber (approximately 0–0.25D) primarily contains existing soil granules, forming a soil retention area within the chamber.

To optimize shield tunneling efficiency, it is crucial to improve the uniformity of granule distribution. This can be achieved by enhancing the internal structure design of the soil chamber. Installing radial mixing bars on the cutterhead main shaft is recommended to improve the flowability of soil granules within the 0–0.25D range in the middle of the soil chamber, preventing blockages and ensuring smoother soil discharge. Such improvements will

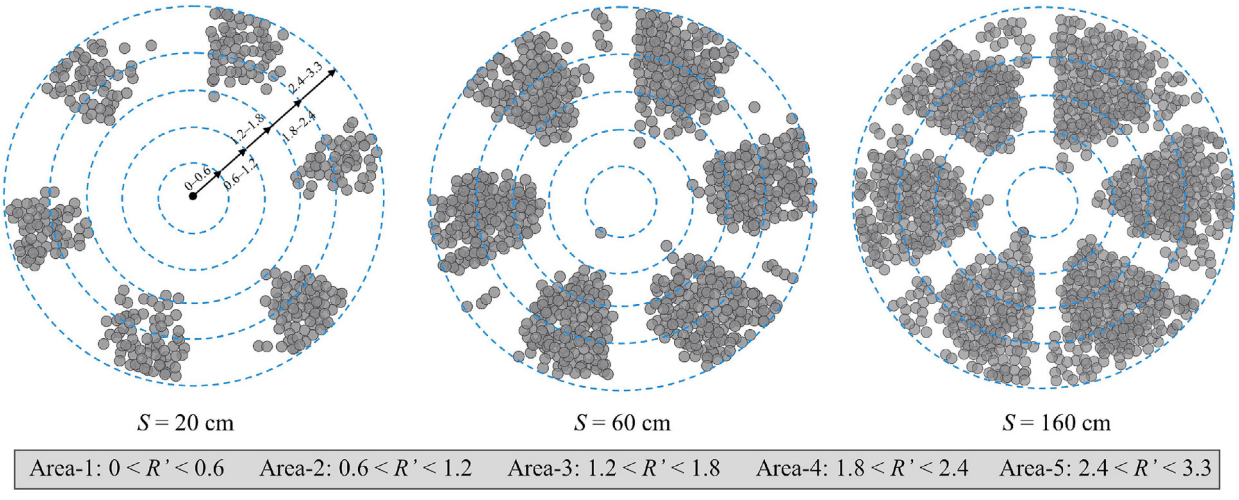

Fig. 30. Soil granule distribution at the soil chamber entrance under different excavation distances. (Unit: m)

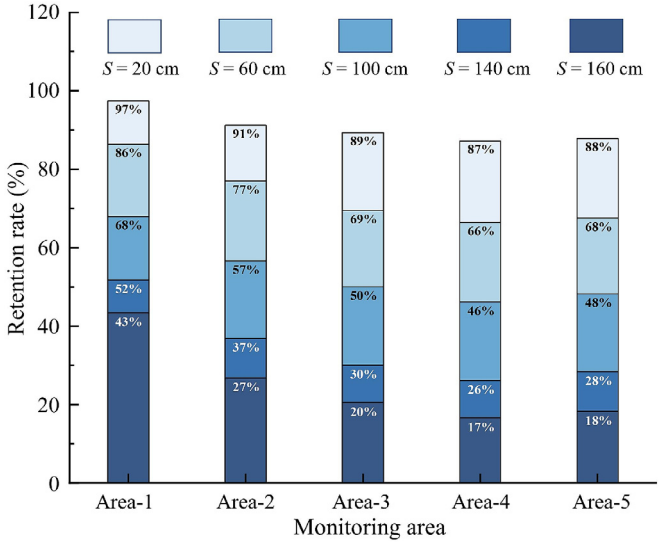

Fig. 31. Variation of soil retention rate in different areas ahead of the cutterhead.

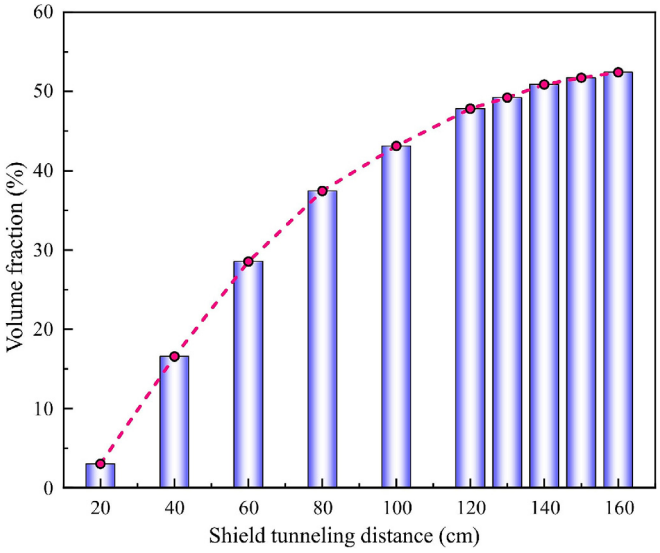

Fig. 33. Volume variation of soil granules entering the soil chamber.

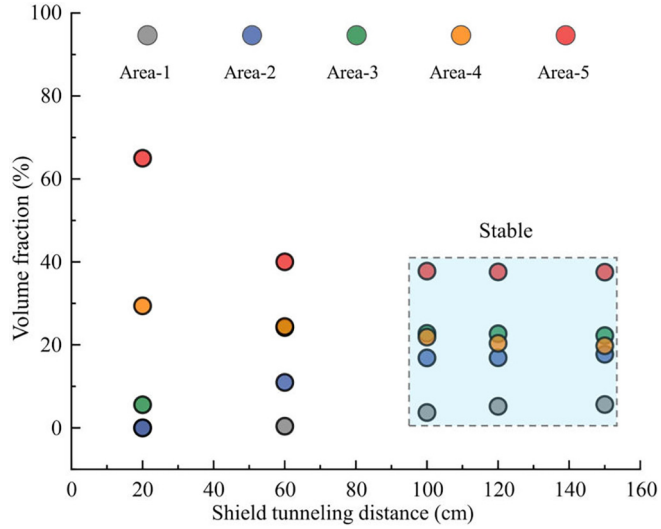

Fig. 32. Volume variation of soil granules entering the soil chamber from different areas.

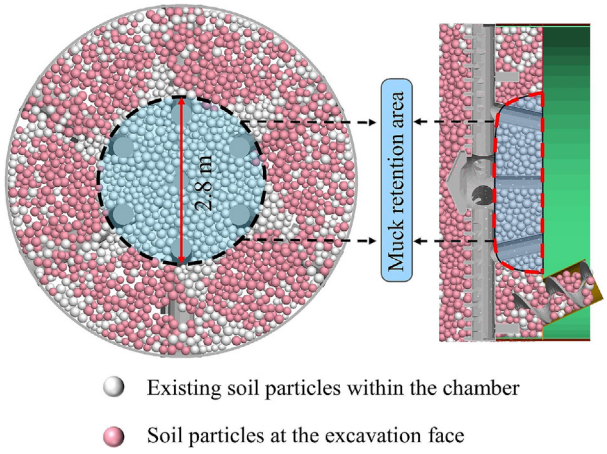

Fig. 34. Soil granule distribution within the soil chamber (S = 150 cm).

increase excavation efficiency, reduce equipment wear, and enhance overall tunneling performance.

5 Conclusions

This study, employing the coupled FDM–DEM method, investigates the spatial motion patterns of sandy cobble granules and the load transfer mechanisms during EPB shield tunneling in sandy cobble strata. The following conclusions are drawn:

(1) A novel gradient stress construction method, based on a rigid wall boundary, is proposed, which significantly improves the accuracy and reliability of the FDM–DEM coupled model.

(2) The soil pressure at the excavation face and within the soil chamber exhibits distinct nonlinear behavior. Specifically, at the excavation face, the soil pressure is lower at the cutterhead spoke positions and higher at the opening. Within the soil chamber, the soil pressure demonstrates a clear radial gradient, with pressure distributions differing on the left and right sides of the chamber due to the rotation of the cutterhead.

(3) In the soil chamber, soil pressure on the left side decreases from top to bottom, while soil pressure on the right side increases. The average pressure in the upper regions of both sides is nearly equal, with the soil pressure transfer coefficient stabilizing at approximately 0.8. This value can serve as a reference for pressure control during tunneling. Practically, an under-pressure advancing strategy is recommended to prevent excessive chamber pressure, based on the-

oretical excavation face pressure values, which could otherwise lead to excessively high support pressure at the excavation face and result in surface uplift damage.

(4) The motion trajectories of sandy cobble granules during tunneling predominantly follow a spiral pattern. In front of the cutterhead, sandy cobble granules within the tail width range experience longer retention times, while granules closer to the cutterhead's outer edge have shorter retention times. The average velocity of granules in the chamber's entrance and middle regions is similar to and greater than that in the area ahead of the cutterhead.

(5) Numerical simulations indicate that sandy cobble granules in the cutterhead center region (0–0.2D) and the central support pillar region (0–0.25D) exhibit lower motion velocities. These regions serve as major retention zones for sandy cobble granules and are prone to clogging. It is therefore suggested that radial stirring rods be installed on the cutterhead spindle to facilitate particle motion. Furthermore, sandy cobble granules entering the chamber from the excavation face primarily accumulate in the region 0.25D–0.50D from the chamber center, where particle flow is higher, facilitating easier discharge from the chamber.

Data availability

The data that support the findings of this study are available from the corresponding author upon reasonable request.

CRediT authorship contribution statement

Yuxiang Yao: Visualization, Validation, Writing – original draft, Data curation. **Yong Fang:** Project administration, Writing – review & editing, Funding acquisition, Resources. **Chuan He:** Resources, Conceptualization, Methodology, Supervision, Funding acquisition. **Gongyun Xu:** Investigation, Formal analysis, Software. **Zhigang Yao:** Investigation, Formal analysis. **Xiongyu Hu:** Resources, Investigation, Formal analysis.

Declaration of competing interest

The authors declare that they have no known competing financial interests or personal relationships that could have appeared to influence the work reported in this paper.

Acknowledgement

This study was supported by the National Science Fund for Distinguished Young Scholars of China (Grant No. 52425807), the Science Foundation of Sichuan Province, China (Grant No. 2024NSFTD0013), the Sichuan "Top Youth" Special Program for Outstanding Young Science and Technology Talent (DQ202403), the National Natural Science Foundation of China (Grant No. 52478418), and the National Natural Science Foundation of China Youth Fund (Grant No. 52408441).

References

Amoun, S., Sharifzadeh, M., Shahriar, K., Rostami, J., & Tarigh Azali, S. (2017). Evaluation of tool wear in EPB tunneling of Tehran metro, line 7 expansion. *Tunnelling and Underground Space Technology, 61*, 233–246.

ASTM (2015). *ASTM C143/C143M: Standard test method for slump of hydraulic-cement concrete*. West Conshohocken, PA: ASTM.

Chen, G. H., Zou, J. F., & Chen, J. Q. (2019). Shallow tunnel face stability considering pore water pressure in non-homogeneous and anisotropic soils. *Computers and Geotechnics, 116*, 103205.

Chen, R. P., Tang, L. J., Ling, D. S., & Chen, Y. M. (2011). Face stability analysis of shallow shield tunnels in dry sandy ground using the discrete element method. *Computers and Geotechnics, 38*(2), 187–195.

Cheng, P. P., Liu, F., Xu, Y. J., & Li, Y. H. (2023). Regulating bulkhead pressure of EPB shield machines through DEM modeling and data mining. *Underground Space, 8*, 15–29.

Dang, T. S., & Meschke, G. (2020). Influence of muck properties and chamber design on pressure distribution in EPB pressure chambers – Insights from computational flow simulations. *Tunnelling and Underground Space Technology, 99*, 103333.

Duan, Z. B., Yang, J., Ma, S. K., & Huang, Z. (2023). Study on instability mechanism of tunnel face in clay-gravel strata under confined water conditions based on DEM-CFD coupling method. *Computers and Geotechnics, 164*, 105769.

Fakhimi, A., Carvalho, F., Ishida, T., & Labuz, J. F. (2002). Simulation of failure around a circular opening in rock. *International Journal of Rock Mechanics and Mining Sciences, 39*(4), 507–515.

Guo, Y. D., Jin, D. L., Li, X. G., Cheng, P. P., Qiao, G. G., Wang, Q. X., & Yang, Y. (2023). Effect of cutting blind zones on the performance of the rectangular pipe jacking machine with multiple cutterheads: A DEM study. *Tunnelling and Underground Space Technology, 134*, 104984.

Hu, Q. X., Wang, S. Y., Qu, T. M., Xu, T., Huang, S., & Wang, H. B. (2020). Effect of hydraulic gradient on the permeability characteristics of foam-conditioned sand for mechanized tunnelling. *Tunnelling and Underground Space Technology, 99*, 103377.

Hu, X. Y., He, C., Fang, Y., Wu, S. Z., & Li, K. J. (2022). Laboratory experiments and discrete element modeling on the surface failure induced by EPB tunneling: The effects of cutterhead open ratio and relative tunneling depth. *Engineering Failure Analysis, 142*, 106731.

Hu, X. Y., He, C., Walton, G., & Fang, Y. (2021). Face stability analysis of EPB shield tunnels in dry granular soils considering nonuniform chamber pressure and a dynamic excavation process. *International Journal of Geomechanics, 21*(6), 04021074.

Idinger, G., Aklik, P., Wu, W., & Borja, R. I. (2011). Centrifuge model test on the face stability of shallow tunnel. *Acta Geotechnica, 6*, 105–117.

Itasca Consulting Group Inc. (2020). Fast Lagrangian Analysis of Continua in 3 Dimensions (FLAC^{3D}). version 7.0. Itasca Consulting Group: Minneapolis, MN, USA, 2020.

Ji, C., Fu, L. L., Zhou, S. H., Yao, Q. Y., & He, C. (2023). Experimental analysis of sand-bearing muck blockages inside single circle earth pressure balance shield chambers. *Tunnelling and Underground Space Technology, 133*, 104907.

Li, T., Zhang, Z. Y., Jia, C. T., Liu, B., Liu, Y. C., & Jiang, Y. S. (2022). Investigating the cutting force of disc cutter in multi-cutter rotary cutting of sandstone: Simulations and experiments. *International Journal of Rock Mechanics and Mining Sciences, 152*, 105069.

Li, X., Xue, Y. G., Li, Z. Q., Kong, F. M., Li, G. K., & Zhou, B. H. (2023). Numerical investigation and prediction of the excavation face stability for river-crossing shield tunneling: An intelligent prediction model for limit support pressure. *Computers and Geotechnics, 160*, 105493.

Lin, Q. T., Lu, D. C., Lei, C. M., Tian, Y., Gong, Q. M., & Du, X. L. (2021). Model test study on the stability of cobble strata during shield under-crossing. *Tunnelling and Underground Space Technology, 110*, 103807.

Liu, B., Li, T., Han, Y. H., Li, D. Y., He, L. L., Fu, C. Q., & Zhang, G. (2022). DEM-continuum mechanics coupling simulation of cutting reinforced concrete pile by shield machine. *Computers and Geotechnics, 152*, 105036.

Ministry of Housing and Urban-Rural Development of the People's Republic of China. (2021). *GB/T 51438—2021: Standard for design of shield tunnel engineering*. Beijing, China: China Architecture & Building Press (in Chinese).

Schöpfer, M. P. J., Abe, S., Childs, C., & Walsh, J. J. (2009). The impact of porosity and crack density on the elasticity, strength and friction of cohesive granular materials: Insights from DEM modelling. *International Journal of Rock Mechanics and Mining Sciences, 46*(2), 250–261.

Shao, X. K., Yang, Z. Y., Jiang, Y. S., & Feng, J. L. (2022). Coupled FDM–DEM method for analyzing EPBS machine tunneling performance in boulders. *International Journal of Geomechanics, 22*(12), 04022239.

Shi, H., Yang, H. Y., Gong, G. F., & Wang, L. T. (2011). Determination of the cutterhead torque for EPB shield tunneling machine. *Automation in Construction, 20*(8), 1087–1095.

Vinai, R., Oggeri, C., & Peila, D. (2008). Soil conditioning of sand for EPB applications: A laboratory research. *Tunnelling and Underground Space Technology, 23*(3), 308–317.

Wan, Z., Li, S. C., Hao, S., Zhao, S. S., & Wang, Z. (2025). Microscopic experiments and numerical simulation of foam-conditioned soil for earth pressure balance shield tunneling in water-rich sandy stratum. *International Journal of Geomechanics, 25*(1), 04024311.

Wu, L., Zhang, X. D., Zhang, Z. H., & Sun, W. C. (2020). 3D discrete element method modelling of tunnel construction impact on an adjacent tunnel. *KSCE Journal of Civil Engineering, 24*, 657–669.

Xie, J. N., Li, P. F., Zhang, M. J., Cao, L. Q., Jia, F., & Li, S. H. (2024). Analytical investigation of the shield-soil rotary friction on tunnelling-induced ground mechanical reactions. *Computers and Geotechnics, 165*, 105922.

Xu, Q. W., Yu, H. F., Chong, J. X., Xie, J. L., He, X., Li, Y. H., & Li, J. (2024). The analysis for characteristic of particles motion and pressure balance stability in the shield soil chamber during the EPBS excavation in weathered diorite stratum. *Engineering Failure Analysis, 159*, 108029.

Yao, Y. X., Fang, Y., Dou, L. P., He, C., Zhuo, B., & Xu, G. Y. (2024). Experimental study on granule trajectory tracking for the EPB shield tunneling in sandy cobble stratum. *Tunnelling and Underground Space Technology, 153*, 105980.

Yi, N. E., & Yang, Y. (2024). Impact of key factors on shield scraper performance in gravelly soil strata: DEM and experimental investigations. *Computers and Geotechnics, 174*, 106592.

Yu, H. J., Mooney, M., & Bezuijen, A. (2020). A simplified excavation chamber pressure model for EPBM tunneling. *Tunnelling and Underground Space Technology, 103*, 103457.

Zhao, D. P., Wang, L. W., Zhang, B. H., Wen, S. X., Li, D., Wang, D. Y., & Fang, H. C. (2022). Study on launch tunnelling parameters of a shield tunnel buried in pebble soil with existing pipelines base on discrete continuous coupling numerical method. *Tunnelling and Underground Space Technology, 129*, 104629.

Zhu, H. H., Cheng, P. P., Zhuang, X. Y., Li, Y. H., & Li, P. N. (2020a). Assessment and structural improvement on the performance of soil chamber system of EPB shield assisted with DEM modeling. *Tunnelling and Underground Space Technology, 96*, 103092.

Zhu, H. X., Yin, Z. Y., & Zhang, Q. (2020b). A novel coupled FDM-DEM modelling method for flexible membrane boundary in laboratory tests. *International Journal for Numerical and Analytical Methods in Geomechanics, 44*(3), 389–404.